Modelling landslide generated waves using the discontinuous finite element method

Wei Pan[a,b], Stephan C. Kramer[b], Matthew D. Piggott[b], Xiping Yu[c,*]

[a]*Department of Hydraulic Engineering, Tsinghua University, Beijing, China*
[b]*Department of Earth Science and Engineering, Imperial College London, London, United Kingdom*
[c]*Department of Ocean Science and Engineering, Southern University of Science and Technology, Shenzhen, China*

Abstract

A new two-layer model for impulsive wave generation by deformable granular landslides is developed based upon a discontinuous Galerkin finite element discretisation. Landslide motion is modelled using a depth-averaged formulation for a shallow subaerial debris flow, which considers the bed curvature represented by the local slope angle variable and accounts for inter-granular stresses using Coulomb friction. Wave generation and propagation are simulated with the three-dimensional non-hydrostatic coastal ocean model *Thetis* to accurately capture key features such as wave dispersion. Two different techniques are used in treating wetting and drying (WD) processes during the landslide displacement and wave generation, respectively. For the lower-layer landslide motion across the dry bed a classical thin-layer explicit WD method is implemented, while for the resulting free-surface waves interacted with the moving landslide an implicit WD scheme is utilised to naturally circumvent the artificial pressure gradient problem which may appear in the dynamic interaction between the landslide and water if using the thin-layer method. The two-layer model is validated using a suite of test cases, with the resulting good agreement demonstrating its capability in describing both the complex behaviours of granular landslides from initiation to deposition, and the consequent wave generation and propagation.

Keywords: Landslide generated wave, Two-layer model, Granular flow, Discontinuous Galerkin, Finite element method, Non-hydrostatic

1. Introduction

Impulsive waves in nature are often related to surface gravity waves caused by a sudden water displacement that may occur in reservoirs, rivers, fjords, and oceans [1]. Apart from earthquakes, landslides are commonly considered as one of the major sources of these waves [2]. These waves are also often referred to as tsunamis in the literature. Past tsunamis, such as those caused by the earthquake in Shikotan in 1994 [3], by the Canadian Grand Banks submarine landslide in 1929 [4], and by the subaerial landslide in Lituya Bay of Alaska in 1958 [5], generated serious humanitarian, economic and environmental impacts in coastal areas. Although significant tsunamis are arguably generated by earthquakes more frequently, landslide generated waves can create the largest hazard [6, 7]. In contrast to earthquakes, subaerial or submarine landslides can generate waves with relatively shorter wavelengths and stronger dispersive characteristics, and locally they may cause higher wave amplitudes and run-up heights along adjacent coastlines. It

*Corresponding author
Email address: yuxp@sustech.edu.cn (Xiping Yu)

should also be noted that it is possible that an earthquake triggers a landslide [8], and that both may contribute to the generation of a tsunami [9–11].

Landslide generated waves represent the combination of two hazards — the landslide itself and any induced (tsunami) waves. For complete numerical simulation one has to consider both the landslide motion, typically with a prescribed rheological assumption, and the coupled and resulting hydrodynamics, including any induced waves. Considerable effort has gone into the study of landslide generated waves using various types of computational models based upon different levels of simplification of the underlying Navier-Stokes equations; for example, the shallow water equations [4, 12–14], Boussinesq wave equation [15–18], and non-hydrostatic pressure decomposed equations [19–22] have been utilised. A computational fluid dynamics (CFD) based approach, e.g. multi-phase flow models solving the full Navier-Stokes equations with a free surface tracking method, is also an alternative approach to accurately reproduce the entire process of the slide motion and its complicated interactions with surrounding water [23–29]. However, its significant computational costs limit the applications of CFD approaches over relatively limited spatial and temporal scales.

In terms of landslide motion, there are generally two approaches taken for large scale simulations. One is to treat the landslide as a rigid solid, potentially with prescribed kinematics obtained from a semi-empirical formulation, while the other is to consider the slide as a deformable object with a particular rheology. In the former the slide motion can be integrated into wave generation/propagation models via an approach that may be interpreted as a moving bottom boundary condition, i.e. one-way coupling where bottom boundary deformations act on the free surface. Although this treatment is widely applied to submarine slides [30–33], and replicates certain simplified lab cases, the inability to capture landslide deformation may limit its application to realistic cases where the deformation of the landslide shape may be important. It should be noted that if the deformation is known a priori it is generally readily feasible to impose it within an otherwise "rigid" block approach [34]. As confirmed by some experimental and numerical studies [35–39], landslide deformation can significantly affect the shape of the slide as well as the impact height and velocity in the case of subaerial slides. The resulting wave amplitudes can be overestimated by models which treat the slide as a solid mass [19, 40–42]. In this sense, allowing the slide to naturally deform can be beneficial for the accurate representation of landslide generated waves.

Among the methodologies available to simulate deformable slides, various rheological models have been used to represent the behaviours of the slides. In terms of submarine landslides, a popular approach is to model the slide and its surrounding water as separate fluids with different properties. For example, based upon the long wave approximation [12] proposed a depth-averaged model where water was taken to be inviscid and incompressible while the deformable slide was treated as a Newtonian, viscous fluid layer. This was further developed and applied to some realistic cases, e.g. in [13] and [43]. Moreover, the slide can also be assumed to be a non-Newtonian fluid, such as by adopting a Bingham rheology [44, 45]. Another alternative approach is to model the slide as a mixture of sediment and water driven by the setting velocity and baroclinic pressure [19, 46, 47].

The deformable landslide and resulting wave generation and propagation can be simulated by the above described approaches and models with reasonable accuracy in the submarine slide case. However, for subaerial slides the fluid based slide models cannot reproduce well the overall landslide motion from the initial sliding on the hillslope to the final deposition, since the laminar viscous fluid or Bingham viscoplastic fluid rheologies cannot properly account for the inter-granular stresses and basal pore water pressure in landslides. Based on depth-averaged formulations for shallow subaerial debris flows

[48–50], numerical models that consider the subaerial landslide as a dense grain-fluid mixture and its motion as debris flow, were applied to describe the granular behaviour of submarine [51–54] and subaerial landslides [20, 21, 55–59]. These models accounted for the inter-granular stresses using a Coulomb friction approach.

In this study we adopt the Savage–Hutter (SH) formulation [48] as that used in [20, 21, 52, 54, 58] to describe the landslide as a granular flow. Different from the models of [20, 21, 58] based on the flat bed-normal coordinate system, the present work follows the formulation of [52, 54], which takes the effects of bottom curvature into account introducing a local slope angle under the hypothesis of small variation of the curvature [60]. In the work presented here, we extend the original two-dimensional (2D) form of equations to the three-dimensional (3D) one with only considering the x-direction bed curvature.

Following the underlying SH theory [48], many granular landslide models were developed and applied, e.g. [20, 21, 51, 52, 54, 55, 58, 59]; however, they are all based on finite volume (FV) or finite difference (FD) methods. To the best of the authors' knowledge this study represents the first application of a finite element based discretisation for modelling tsunami wave generation from granular landslides based upon the SH theory.

In the context of more general landslide-induced wave applications, recent advances in particle or meshless methods should be acknowledged that are also suited to this type of problem [61–66]. Although this kind of approach allows for the more accurate representation of the constitutive relation among the material particles within the landslide, it is still a challenge to directly apply meshfree particle methods to large-scale applications due in part to significant computational costs and the disparity between horizontal and vertical lengths scales. The work in this study, presenting one of the first demonstrations of the discontinuous Galerkin based finite element (DG-FE) discretisation, hence focuses on mesh based modelling.

A DG-FE based two-layer granular landslide and wave generation coupled model is thus developed within the coastal ocean model *Thetis* [22, 47, 67–69]. For this work one of the main objectives is to introduce an applicable two-layer model applying the discontinuous Galerkin method to the modelling of granular landslide generated waves. The DG method offers high-order accuracy, is strictly conservative locally, while also inheriting the geometric flexibility of FE and FV methods [47]. During the whole processes of subaerial landslide motion and its generated wave run-up, significant wetting and drying (WD) processes occur and thus efficient WD methods are required to accurately capture the moving WD front. In this work, a well-balanced vertex-based WD method [70, 71], compatible with the Runge-Kutta DG-FE based approximation, is implemented in *Thetis* combined with a Harten–Lax–van Leer–Contact (HLLC) Riemann solver [72] resolving the dry bed flux especially at the WD front during granular landslide movement.

The remainder of the paper is structured as follows. The governing equations for both the granular landslide and wave generation are presented in Section 2. The finite element discretisation, time integration scheme and wetting and drying techniques are introduced in Section 3. Numerical benchmarking against several test cases is demonstrated in Section 4, followed by conclusions in Section 5.

2. Mathematical formulation

In this work, a two-layer model is developed for granular landslide generated waves. Landslide motion (the lower-layer) is represented through a depth-averaged granular model, while wave generation and propagation (the upper-layer) are modelled using the three-dimensional coastal ocean model *Thetis*. The formulations for this coupled system are presented separately in this section.

2.1. Lower-layer granular landslide

Following [73], the landslide motion is treated via the flow of a grain-fluid Coulomb mixture. Assuming the flow is incompressible, the starting system of equations in the Cartesian coordinate system read

$$\nabla \cdot \mathbf{v} = 0, \tag{1}$$

$$\rho\left(\frac{\partial \mathbf{v}}{\partial t} + \mathbf{v} \cdot \nabla \mathbf{v}\right) = -\nabla \cdot \mathbf{T} + \rho \nabla (\mathbf{g} \cdot \mathbf{x}), \tag{2}$$

in which

$$\rho = \gamma^s \rho^s + \gamma^f \rho^f, \qquad \mathbf{v} = \left(\gamma^s \rho^s \mathbf{v}^s + \gamma^f \rho^f \mathbf{v}^f\right)/\rho, \qquad \mathbf{T} = \mathbf{T}^s + \mathbf{T}^f. \tag{3}$$

Here ρ is the mixture density, and $\mathbf{v} = [v_x, v_y, v_z]^T$ is the mixture velocity. $\mathbf{g} = [0, 0, -g]^T$ represents the gravitational acceleration. $\mathbf{x} = (x, y, z)$ denotes Cartesian coordinate, and $\nabla = [\frac{\partial}{\partial x}, \frac{\partial}{\partial y}, \frac{\partial}{\partial z}]$ is the gradient operator in the Cartesian coordinate system. $\mathbf{T}$ is the stress tensor and normal stresses are defined as positive in compression. It is assumed that the granular quantities have contributions from both the solid and fluid phases denoted by the superscript 's' and 'f', respectively, and both phases have the same velocity [73]. Those variables with no superscript represent the final mixture of solid and fluid phases with corresponding volume fractions γ^s and γ^f, respectively, where $\gamma^s + \gamma^f = 1$.

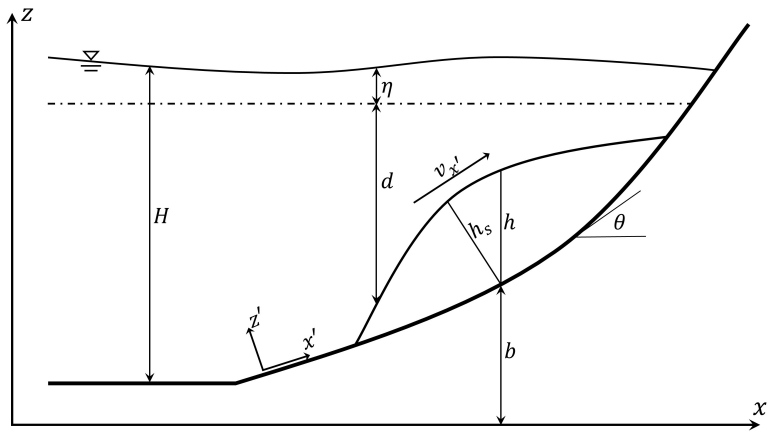


Figure 1: Sketch of the two-layer system with model parameters defined. The lower-layer landslide motion is along the non-erodible bottom b with the curvature represented by the local slope angle θ.

Equations (1) and (2) are then transferred to a local coordinate system over the non-flat bed denoted by $z = b(x)$. For the sake of simplicity, this study only considers the $x-$direction bed curvature with a local slope angle θ (see Fig. 1). We simply extend the two-dimensional transformation matrix in [52] to the following three-dimensional one,

$$\nabla_{\mathbf{x}}(x', z') = \frac{1}{J}\begin{bmatrix} \cos\theta & 0 & \sin\theta \\ 0 & J & 0 \\ -J\sin\theta & 0 & J\cos\theta \end{bmatrix}, \qquad J = 1 - z'\frac{d\theta}{dx'}, \tag{4}$$

where θ is only related to the $x'-$ and $z'-$ components of the local coordinate system $\mathbf{x}' = (x', y', z')$. x' represents the curve length of the bottom, and z' denotes the distance measured perpendicular to the bottom. J is the Jacobian of the change of variables, and

for a non-erodible bed $\frac{d\theta}{dx'} = \frac{\partial\theta}{\partial x'}$ is valid. Following [52], the transferred equations in the new local coordinate system are

$$\frac{\partial v_{x'}}{\partial x'} + \frac{\partial J v_{y'}}{\partial y'} + \frac{\partial J v_{z'}}{\partial z'} = 0, \tag{5}$$

$$\rho\left[\frac{\partial J v_{x'}}{\partial t} + \frac{\partial v_{x'}^2}{\partial x'} + \frac{\partial J v_{x'} v_{y'}}{\partial y'} + \frac{\partial J v_{x'} v_{z'}}{\partial z'}\right] = \rho\frac{\partial(\mathbf{g}\cdot\mathbf{x})}{\partial x'} - \frac{\partial T_{x'x'}}{\partial x'} - \frac{\partial J T_{y'x'}}{\partial y'} - \frac{\partial J T_{z'x'}}{\partial z'} + \rho v_{z'}\left(\frac{\partial v_{x'}\theta}{\partial x'} + \frac{\partial J v_{y'}\theta}{\partial y'} + \frac{\partial J v_{z'}\theta}{\partial z'}\right) + T_{x'z'}\frac{d\theta}{dx'}, \tag{6}$$

$$\rho\left[\frac{\partial J v_{y'}}{\partial t} + \frac{\partial v_{x'} v_{y'}}{\partial x'} + \frac{\partial J v_{y'}^2}{\partial y'} + \frac{\partial J v_{y'} v_{z'}}{\partial z'}\right] = -\frac{\partial T_{x'y'}}{\partial x'} - \frac{\partial J T_{y'y'}}{\partial y'} - \frac{\partial J T_{z'y'}}{\partial z'}, \tag{7}$$

$$\rho\left[\frac{\partial J v_{z'}}{\partial t} + \frac{\partial v_{x'} v_{z'}}{\partial x'} + \frac{\partial J v_{y'} v_{z'}}{\partial y'} + \frac{\partial J v_{z'}^2}{\partial z'}\right] = \rho J\frac{\partial(\mathbf{g}\cdot\mathbf{x})}{\partial z'} - \frac{\partial T_{x'z'}}{\partial x'} - \frac{\partial J T_{y'z'}}{\partial y'} - \frac{\partial J T_{z'z'}}{\partial z'} - \rho v_{x'}\left(\frac{\partial v_{x'}\theta}{\partial x'} + \frac{\partial J v_{y'}\theta}{\partial y'} + \frac{\partial J v_{z'}\theta}{\partial z'}\right) - T_{x'x'}\frac{d\theta}{dx'}, \tag{8}$$

where $v_{x'}$, $v_{y'}$ and $v_{z'}$ are the velocity components based on the local slope coordinate. Note that no coordinate transformation terms are present in (7), since no $y-$direction bed curvature is considered in the present work for simplicity. The coordinate transformation terms in (6) and (8) can also be further clarified as follows

$$\rho v_{z'}\left(\frac{\partial v_{x'}\theta}{\partial x'} + \frac{\partial J v_{y'}\theta}{\partial y'} + \frac{\partial J v_{z'}\theta}{\partial z'}\right) = \rho v_{x'} v_{z'}\frac{d\theta}{dx'}, \tag{9}$$

$$\rho v_{x'}\left(\frac{\partial v_{x'}\theta}{\partial x'} + \frac{\partial J v_{y'}\theta}{\partial y'} + \frac{\partial J v_{z'}\theta}{\partial z'}\right) = \rho v_{x'}^2\frac{d\theta}{dx'}, \tag{10}$$

which is valid given that no bed curvature in the $y-$direction is considered.

For the landslide layer, kinematic boundary conditions at the slide surface ($z' = h_s$) and the non-erodible bottom ($z' = 0$) are given by

$$v_{z'} = \frac{\partial h_s}{\partial t} + v_{x'}\frac{\partial h_s}{\partial x'} + v_{y'}\frac{\partial h_s}{\partial y'} \qquad \text{at} \quad z' = h_s, \tag{11}$$

$$v_{z'} = 0 \qquad \text{at} \quad z' = 0, \tag{12}$$

and dynamic boundary conditions are [54]

$$\mathbf{n}_i \cdot \left(\mathbf{T}^{(1)} - \mathbf{T}^{(2)}\right)\mathbf{n}_i = 0 \qquad \text{at} \quad z' = h_s, \tag{13}$$

$$\mathbf{T}^{(2)}\mathbf{n}_b - \left(\left(\mathbf{T}^{(2)}\mathbf{n}_b\right)\cdot\mathbf{n}_b\right)\mathbf{n}_b = \begin{pmatrix} -\mathbf{n}_b\cdot\left(\mathbf{T}^{(2)} - \mathbf{T}^{(1)}\right)\mathbf{n}_b \frac{v_{x'}}{\sqrt{v_{x'}^2 + v_{y'}^2}}\tan\phi_b \\ -\mathbf{n}_b\cdot\left(\mathbf{T}^{(2)} - \mathbf{T}^{(1)}\right)\mathbf{n}_b \frac{v_{y'}}{\sqrt{v_{x'}^2 + v_{y'}^2}}\tan\phi_b \\ 0 \end{pmatrix} \qquad \text{at} \quad z' = 0, \tag{14}$$

where h_s is the thickness of landslide perpendicular to the bottom. $\mathbf{n}_i$ and $\mathbf{n}_b$ are the exterior unit normal vectors at the slide-water interface and the bottom, respectively. The superscript $^{(1)}$ and $^{(2)}$ denote the upper water layer and the lower slide layer, respectively. ϕ_b is the basal friction angle, and it is noted that the Coulomb-type friction law presented in (14) takes into account the buoyancy effects from the fluid layer where grains are submerged.

Next, the model equations (5)–(8) are integrated in the direction normal to the bed. In the integration process, $\frac{d\theta}{dx'}$ is assumed to be $O(\epsilon)$ [52] ($\epsilon = H'/L'$ with H' and L' representing the characteristic lengths in the x' and z' directions), and $z'\frac{d\theta}{dx'}$ is supposed to

be small. $J = 1 - z'\frac{d\theta}{dx'}$ is then reduced to $J = 1$ up to second order, and hence we drop J in the following derivation. The underlying hypothesis is based on small variations of the bed curvature considered in this study. For the test cases that meet the criteria of small variations of bed curvature, it can be expected that reducing J to second order does not affect the accuracy of the results. Similarly, the integration of the term $T_{x'z'}\frac{d\theta}{dx'}$ in (6), i.e.

$$\int_0^{h_s} T_{x'z'}\frac{d\theta}{dx'}dz' = T_{x'z'}\left[z\frac{d\theta}{dx'}\right]_{z'=0}^{z'=h_s},$$

is also supposed to be a small value compared with other terms, and can be dropped here.

Using the boundary conditions, integrating (5)–(7) over the slide thickness, and dropping high-order terms as in [52, 54], we obtain the depth-integrated continuity and horizontal momentum equations

$$\frac{\partial h_s}{\partial t} + \frac{\partial h_s\bar{v}_{x'}}{\partial x'} + \frac{\partial h_s\bar{v}_{y'}}{\partial y'} = 0, \tag{15}$$

$$\rho\left[\frac{\partial h_s\bar{v}_{x'}}{\partial t} + \frac{\partial h_s\bar{v}_{x'}^2}{\partial x'} + \frac{\partial h_s\bar{v}_{x'}\bar{v}_{y'}}{\partial y'}\right] = \int_0^{h_s}\rho\frac{\partial(\mathbf{g}\cdot\mathbf{x})}{\partial x'}dz' - \int_0^{h_s}\left[\frac{\partial T_{x'x'}}{\partial x'} + \frac{\partial T_{y'x'}}{\partial y'} + \frac{\partial T_{z'x'}}{\partial z'}\right]dz', \tag{16}$$

$$\rho\left[\frac{\partial h_s\bar{v}_{y'}}{\partial t} + \frac{\partial h_s\bar{v}_{x'}\bar{v}_{y'}}{\partial x'} + \frac{\partial h_s\bar{v}_{y'}^2}{\partial y'}\right] = -\int_0^{h_s}\left[\frac{\partial T_{x'y'}}{\partial x'} + \frac{\partial T_{y'y'}}{\partial y'} + \frac{\partial T_{z'y'}}{\partial z'}\right]dz', \tag{17}$$

where $\bar{v}_{x'}$ and $\bar{v}_{y'}$ are depth-averaged velocities in the x' and y' directions, respectively. Note that the over-bar notation implies a depth-average quantity throughout.

Given the much larger 'horizontal' length scale of most of the slide scenarios under consideration are in comparison to the 'vertical', the vertical momentum equation can be first reduced to

$$\frac{\partial T_{z'z'}}{\partial z'} = \rho\frac{\partial(\mathbf{g}\cdot\mathbf{x})}{\partial z'} - \rho v_{x'}^2\frac{d\theta}{dx'}, \tag{18}$$

i.e.

$$\begin{aligned}\frac{\partial T^s_{z'z'}}{\partial z'} + \frac{\partial T^f_{z'z'}}{\partial z'} &= \rho\frac{\partial[-g(b+z'\cos\theta)]}{\partial z'} - \rho v_{x'}^2\frac{d\theta}{dx'}\\ &= -\rho g\cos\theta - \rho v_{x'}^2\frac{d\theta}{dx'},\end{aligned} \tag{19}$$

where $T^s_{z'z'}$ and $T^f_{z'z'}$ are z'-direction normal stresses in solid and fluid phases, respectively. Then integrating (19) over the landslide depth, we obtain

$$T^s_{z'z'}|_{z'=0} = \rho g h_s\cos\theta + \rho h_s\bar{v}_{x'}^2\frac{d\theta}{dx'} + T^s_{z'z'}|_{z'=h_s} + T^f_{z'z'}|_{z'=h_s} - T^f_{z'z'}|_{z'=0}. \tag{20}$$

For the sake of simplicity, $|_{z'=0}$ and $|_{z'=h_s}$ are replaced by subscripts 'b' and 'h' denoting the bed and landslide-water interface, respectively, and hence (20) becomes

$$T^s_{z'z'b} = \rho g h_s\cos\theta + \rho h_s\bar{v}_{x'}^2\frac{d\theta}{dx'} + T^s_{z'z'h} + T^f_{z'z'h} - T^f_{z'z'b}. \tag{21}$$

Given the upper-layer fluid pressure at the interface $P^f_h = T^s_{z'z'h} + T^f_{z'z'h}$, a distribution factor λ_1 is introduced to describe the contribution from the fluid and solid phases of the lower layer [52], i.e. $T^f_{z'z'h} = \lambda_1 P^f_h$ and $T^s_{z'z'h} = (1-\lambda_1)P^f_h$. Furthermore, assuming

the pressure in the fluid phase is linearly dependent on the landslide depth, the pore pressure at the bed can be related to that at the interface via

$$T^f_{z'z'b} = T^f_{z'z'h} + \lambda_2 \rho^f g h_s \cos\theta, \tag{22}$$

and the depth-averaged pressure is

$$\bar{T}^f_{z'z'} = \frac{1}{2}\left(T^f_{z'z'b} + T^f_{z'z'h}\right) = \lambda_1 P^f_h + \frac{1}{2}\lambda_2 \rho^f g h_s \cos\theta, \tag{23}$$

where λ_2 is another factor defined by [49] to control what percent of the normal pressure comes from fluid phase through the lower granular layer. Both the factors λ_1 and λ_2 are determined through calibration such as laboratory measurements. Note that $\lambda_1 = 0$ implies the isolation of the pore fluid from the upper water layer, while $\lambda_1 = 1$ represents the continuity of the fluid pressure between the lower grain-fluid mixture layer and the upper water layer.

Substituting (22) into (21), the normal stress in the solid phase at the bed is given by

$$T^s_{z'z'b} = (1-\lambda_1)P^f_h + \left(\rho - \lambda_2 \rho^f\right) g h_s \cos\theta + \rho h_s \bar{v}^2_{x'} \frac{d\theta}{dx'}, \tag{24}$$

and the depth-averaged value is

$$\bar{T}^s_{z'z'} = (1-\lambda_1)P^f_h + \frac{1}{2}\left(\rho - \lambda_2 \rho^f\right) g h_s \cos\theta + \frac{1}{2}\rho h_s \bar{v}^2_{x'} \frac{d\theta}{dx'}. \tag{25}$$

The stresses in the x'-direction momentum equation can be formulated as follows

$$\begin{aligned} -\int_0^{h_s}\left[\frac{\partial T_{x'x'}}{\partial x'} + \frac{\partial T_{y'x'}}{\partial y'} + \frac{\partial T_{z'x'}}{\partial z'}\right]dz' = &-\left[\frac{\partial\left(h_s \bar{T}_{x'x'}\right)}{\partial x'} + \frac{\partial\left(h_s \bar{T}_{y'x'}\right)}{\partial y'}\right] \\ &+ \frac{\partial h_s}{\partial x'} T_{x'x'h} + \frac{\partial h_s}{\partial y'} T_{y'x'h} + T_{z'x'b} - T_{z'x'h}, \end{aligned} \tag{26}$$

in which the Leibniz integral rule is applied. Constitutive relations can be applied to relate normal and shear stresses of each phase. The fluid phase of the Coulomb mixture is assumed as homogeneous and an isotropic stress is defined, i.e. $T^f_{x'x'} = T^f_{y'y'} = T^f_{z'z'}$. In terms of the anisotropic solid phase, the normal stresses $T^s_{x'x'}$ and $T^s_{y'y'}$ are related to the z'-direction normal stress $T^s_{z'z'}$ through a coefficient of lateral earth pressure $k_{a/p}$ derived from Coulomb theory:

$$T^s_{x'x'} = T^s_{y'y'} = k_{a/p} T^s_{z'z'}. \tag{27}$$

For frictional granular material, the earth pressure coefficient $k_{a/p}$ (sometimes represented by $k_{act/pas}$ in literature) can be taken to be [48, 49]

$$k_{a/p} = \begin{cases} 2\dfrac{1\mp\left[1-\cos^2\phi_i\left(1+\tan^2\phi_b\right)\right]^{1/2}}{\cos^2\phi_i} - 1 & \text{if } \phi_i \geq \phi_b, \\ \dfrac{1+\sin^2\phi_i}{1-\sin^2\phi_i} & \text{if } \phi_i < \phi_b, \end{cases} \tag{28}$$

where ϕ_i is the internal friction angle, and ϕ_b is the basal friction angle. For divergent depth-averaged flow which is indicated by $\frac{\partial \bar{v}_{x'}}{\partial x'} + \frac{\partial \bar{v}_{y'}}{\partial x'} > 0$, the sign $\mp$ is negative and $k_{a/p}$ corresponds to k_{act}; for convergent flow the sign $\mp$ is positive and $k_{a/p}$ corresponds to k_{pas}. In terms of $\frac{\partial \bar{v}_{x'}}{\partial x'} + \frac{\partial \bar{v}_{y'}}{\partial x'} = 0$, $k_{a/p} = (k_{act} + k_{pas})/2$ can be considered for this case and hence $k_{a/p} = 1 + \tan^2\phi_i$ [52].

Assuming that all stresses inside the landslide increase linearly with landslide thickness, we obtain

$$T_{x'x'h} = k_{a/p} T^s_{z'z'h} + T^f_{z'z'h} = \Big(\lambda_1 + k_{a/p}\,(1-\lambda_1)\Big) P^f_h, \tag{29}$$

and the depth-averaged normal ones

$$\begin{aligned}\bar{T}_{x'x'} &= k_{a/p}\bar{T}^s_{z'z'} + \bar{T}^f_{z'z'} \\ &= \Big(\lambda_1 + k_{a/p}\,(1-\lambda_1)\Big) P^f_h + \frac{1}{2}\Big(\lambda_2\rho^f + k_{a/p}\Big(\rho - \lambda_2\rho^f\Big)\Big) g h_s \cos\theta + \frac{1}{2} k_{a/p}\rho h_s \bar{v}^2_{x'} \frac{d\theta}{dx'}.\end{aligned} \tag{30}$$

The shear stresses $T_{y'x'}$ in (26) can also be expressed as [20]

$$T_{y'x'} = -\mathrm{sign}(S_{x'y'}) T^s_{x'x'} \sin\phi_i, \tag{31}$$

where $S_{x'y'}$ is the rate of strain indicated by $\frac{1}{2}(\frac{\partial \bar{v}_{x'}}{\partial y'} + \frac{\partial \bar{v}_{y'}}{\partial x'})$, and note that the fluid shear stress are negligible as compared with the Coulomb friction they are insignificant. Similarly, we obtain

$$T_{y'x'h} = -\mathrm{sign}(S_{x'y'}) k_{a/p}\,(1-\lambda_1)\, P^f_h \sin\phi_i, \tag{32}$$

$$\bar{T}_{y'x'} = -\mathrm{sign}(S_{x'y'}) k_{a/p}\left[(1-\lambda_1) P^f_h + \frac{1}{2}\Big(\rho - \lambda_2\rho^f\Big) g h_s \cos\theta + \frac{1}{2}\rho h_s \bar{v}^2_{x'} \frac{d\theta}{dx'}\right] \sin\phi_i. \tag{33}$$

Furthermore, the Coulomb-type friction law gives the shear stress at the bed

$$T_{z'x'b} = -T^s_{z'z'b} \frac{\bar{v}_{x'}}{|\bar{\mathbf{v}}|} \tan\phi_b = -\left[(1-\lambda_1) P^f_h + \Big(\rho - \lambda_2\rho^f\Big) g h_s \cos\theta + \rho h_s \bar{v}^2_{x'} \frac{d\theta}{dx'}\right] \frac{\bar{v}_{x'}}{\sqrt{\bar{v}^2_{x'} + \bar{v}^2_{y'}}} \tan\phi_b. \tag{34}$$

The shear stress at the layer interface $T_{z'x'h}$ and $T_{z'y'h}$ are represented by the friction between the upper and lower layers [52]:

$$\mathrm{fric}_x\Big(\boldsymbol{u}^f_d, \bar{\mathbf{v}}\Big) = -\rho^f K_{\mathrm{in}} \Big|\boldsymbol{u}^f_d - \bar{\mathbf{v}}\Big| \Big(u^f_d - \bar{v}_{x'}\Big), \tag{35}$$

$$\mathrm{fric}_y\Big(\boldsymbol{u}^f_d, \bar{\mathbf{v}}\Big) = -\rho^f K_{\mathrm{in}} \Big|\boldsymbol{u}^f_d - \bar{\mathbf{v}}\Big| \Big(v^f_d - \bar{v}_{y'}\Big), \tag{36}$$

where $\boldsymbol{u}^f_d = [u^f_d, v^f_d]^T$ stands for the upper-layer fluid velocity near the landslide-water interface, and K_{in} is a positive constant.

The gravity based term in the x'-direction momentum equation is evaluated as follows

$$\begin{aligned}\int_0^{h_s} \rho \frac{\partial(\mathbf{g}\cdot\mathbf{x})}{\partial x'} dz' &= \int_0^{h_s} \rho \frac{\partial[-g(b + z'\cos\theta)]}{\partial x'} dz' \\ &= -\rho g h_s \frac{\partial b}{\partial x'} + \frac{1}{2}\rho g h_s^2 \sin\theta \frac{d\theta}{dx'}.\end{aligned} \tag{37}$$

Note that the term in (9) containing the vertical velocity vanishes in the integration process due to the shallow domain considered.

Analogously, all the stresses in the y' direction in the depth-averaged momentum equation can be obtained. Then substituting all evaluated terms, and re-transforming the model equations to the Cartesian coordinate system based on the following relations,

$$\frac{\partial}{\partial x'} = \cos\theta \frac{\partial}{\partial x}, \qquad \frac{\partial}{\partial y'} = \frac{\partial}{\partial y}, \qquad h = \frac{h_s}{\cos\theta}, \qquad p = h\bar{v}_{x'}, \qquad q = h\bar{v}_{y'}, \tag{38}$$

we finally obtain the granular flow equations in divergence form in the Cartesian coordinate system

$$\frac{\partial \mathbf{W}}{\partial t} + \nabla_h \cdot \mathbf{F}(\theta, \mathbf{W}) = \mathbf{S}(\theta, \mathbf{W}), \tag{39}$$

where $\nabla_h = [\frac{\partial}{\partial x}, \frac{\partial}{\partial y}]$ is the horizontal gradient operator, $\mathbf{W}$ is a vector defined as $\mathbf{W} \equiv [h, p, q]^T$, and the flux matrix $\mathbf{F} = [\mathbf{F}_x, \mathbf{F}_y]$ are given by

$$\mathbf{F}_x = \begin{bmatrix} p\cos\theta \\ \frac{p^2}{h}\cos\theta + \frac{1}{2}\Lambda_2 g h^2 \cos^3\theta \\ \frac{pq}{h}\cos\theta \end{bmatrix}, \qquad \mathbf{F}_y = \begin{bmatrix} q \\ \frac{pq}{h} \\ \frac{q^2}{h} + \frac{1}{2}\Lambda_2 g h^2 \cos^2\theta \end{bmatrix}, \tag{40}$$

with $\Lambda_1 = \lambda_1 + k_{a/p}(1-\lambda_1)$, $\Lambda_2 = r\lambda_2 + k_{a/p}(1-r\lambda_2)$ and $r = \frac{\rho^f}{\rho}$.

The source term is $\mathbf{S} = \mathbf{S}_g + \mathbf{S}_\tau + \mathbf{S}_c$. The gravity related term $\mathbf{S}_g$ and the coupling term between the upper and lower layer $\mathbf{S}_c$ are given by

$$\mathbf{S}_g = \begin{bmatrix} 0 \\ -gh\cos\theta\frac{\partial b}{\partial x} - \frac{1}{4}gh^2\cos\theta\frac{\partial \cos^2\theta}{\partial x} \\ 0 \end{bmatrix}, \qquad \mathbf{S}_c = \begin{bmatrix} 0 \\ -\frac{\Lambda_1}{\rho}h\cos\theta\frac{\partial P_h^f}{\partial x} - \frac{\mathrm{fric}_x}{\rho\cos\theta} \\ -\frac{\Lambda_1}{\rho}h\frac{\partial P_h^f}{\partial y} - \frac{\mathrm{fric}_y}{\rho\cos\theta} \end{bmatrix}, \tag{41}$$

and $\mathbf{S}_\tau = [0, S_{\tau x}, S_{\tau y}]^T$ is the main stress term, in which

$$\begin{aligned} S_{\tau x} = &-\left[\frac{(1-\lambda_1)P_h^f}{\rho\cos\theta} + (1-r\lambda_2)gh\cos\theta + \frac{p^2}{h}\frac{\partial \sin\theta}{\partial x}\right]\frac{p}{\sqrt{p^2+q^2}}\tan\phi_b \\ &+ \mathrm{sign}(S_{xy})k_{a/p}h\left[\frac{1-\lambda_1}{\rho}\frac{\partial P_h^f}{\partial y} + (1-r\lambda_2)g\frac{\partial h\cos^2\theta}{\partial y}\right]\sin\phi_i, \end{aligned} \tag{42}$$

$$\begin{aligned} S_{\tau y} = &-\left[\frac{(1-\lambda_1)P_h^f}{\rho\cos\theta} + (1-r\lambda_2)gh\cos\theta + \frac{p^2}{h}\frac{\partial \sin\theta}{\partial x}\right]\frac{q}{\sqrt{p^2+q^2}}\tan\phi_b \\ &+ \mathrm{sign}(S_{xy})k_{a/p}h\left[\frac{1-\lambda_1}{\rho}\cos\theta\frac{\partial P_h^f}{\partial x} + (1-r\lambda_2)g\cos\theta\frac{\partial h\cos^2\theta}{\partial x}\right]\sin\phi_i. \end{aligned} \tag{43}$$

It should be noted that under the hypothesis of small variations of the bed curvature considered here the higher-order residual terms related to bed curvature in the coordinate transformation have been dropped as in the dimensional analysis of [52, 54].

2.2. Upper-layer wave generation

The landslide wave generation and its subsequent propagation are modelled using a non-hydrostatic (NH) version of the 3D DG-FE based coastal ocean model *Thetis* [22, 47, 68]. A series of NH formulations are included in *Thetis*, including a multi-layer model [68], an Arbitrary Lagrangian Eulerian (ALE) based model [22] and a σ-coordinate based model [47], all of which can accurately simulate the free-surface water waves present in the upper-layer. In [47], it is demonstrated that the multi-layered approach is fully consistent with the σ-coordinate formulation with a specific vertically discretised form

of model equations, and that the σ-transformation approach can be considered equivalent to the ALE approach with a particular type of mapping. The current work hence adopts the σ-coordinate based model for the representation of the upper-layer free-surface waves.

The governing equations, i.e. the 3D incompressible Navier-Stokes equations, are transformed into a σ-coordinate system based on the relations [74, 75]

$$t = t^*, \qquad x = x^*, \qquad y = y^*, \qquad \sigma = \frac{z^* + d}{H}, \tag{44}$$

where (x^*, y^*, z^*) denotes the standard 3D Cartesian coordinate system and (x, y, σ) represents the target domain where the wave model equations are solved.

Dropping the Coriolis, baroclinic pressure and viscosity terms which are not relevant to this study, the continuity and momentum equations in the σ-coordinate system take the form

$$\frac{\partial u}{\partial x} + \frac{\partial u}{\partial \sigma}\frac{\partial \sigma}{\partial x^*} + \frac{\partial v}{\partial y} + \frac{\partial v}{\partial \sigma}\frac{\partial \sigma}{\partial y^*} + \frac{\partial w}{\partial \sigma}\frac{\partial \sigma}{\partial z^*} = 0, \tag{45}$$

$$\frac{\partial u}{\partial t} + u\frac{\partial u}{\partial x} + v\frac{\partial u}{\partial y} + \omega\frac{\partial u}{\partial \sigma} + g\frac{\partial \eta}{\partial x} = -\frac{1}{\rho^f}\left(\frac{\partial Q}{\partial x} + \frac{\partial Q}{\partial \sigma}\frac{\partial \sigma}{\partial x^*}\right), \tag{46}$$

$$\frac{\partial v}{\partial t} + u\frac{\partial v}{\partial x} + v\frac{\partial v}{\partial y} + \omega\frac{\partial v}{\partial \sigma} + g\frac{\partial \eta}{\partial y} = -\frac{1}{\rho^f}\left(\frac{\partial Q}{\partial y} + \frac{\partial Q}{\partial \sigma}\frac{\partial \sigma}{\partial y^*}\right), \tag{47}$$

$$\frac{\partial w}{\partial t} + u\frac{\partial w}{\partial x} + v\frac{\partial w}{\partial y} + \omega\frac{\partial w}{\partial \sigma} = -\frac{1}{\rho^f}\frac{\partial Q}{\partial \sigma}\frac{\partial \sigma}{\partial z^*}, \tag{48}$$

with

$$\frac{\partial \sigma}{\partial t^*} = -\frac{\partial \sigma}{\partial z^*}\frac{\partial z^*}{\partial t}, \quad \frac{\partial \sigma}{\partial x^*} = -\frac{\partial \sigma}{\partial z^*}\frac{\partial z^*}{\partial x}, \quad \frac{\partial \sigma}{\partial y^*} = -\frac{\partial \sigma}{\partial z^*}\frac{\partial z^*}{\partial y}, \quad \frac{\partial \sigma}{\partial z^*} = \frac{1}{H}, \tag{49}$$

and the vertical velocity that arises in the σ-coordinate, given by

$$\omega = \frac{D\sigma}{Dt^*} = \frac{\partial \sigma}{\partial t^*} + u\frac{\partial \sigma}{\partial x^*} + v\frac{\partial \sigma}{\partial y^*} + w\frac{\partial \sigma}{\partial z^*}, \tag{50}$$

where $[u, v, w]^T$ is the 3D velocity vector and Q is the non-hydrostatic component of the total pressure. d is the water depth from the slide surface to the still water level and $H = \eta + d$ is the total depth with η denoting the free-surface elevation. More details of the free-surface flow model can be found in [22].

2.3. Interaction between landslide and water

At the wave generation stage, the landslide deformation can significantly contribute to the surrounding water fluctuation and vice versa. For an accurate representation of the landslide-wave processes, their interaction should be treated properly. While retaining sufficient accuracy in simulating slide motion and its generated waves, the coupled model presented in this work simplifies the interaction such that the mixing effects at the landslide-water interface are not considered, e.g. the entrainment of large air cavities are ignored. The landslide and surrounding water are assumed to remain in contact. Furthermore it is noted that significant wetting and drying processes are involved and should be handled accurately. The specific numerical technique will be presented in section 3.3 about wetting and drying treatments.

The coupling of the slide motion and free-surface flow is mainly through the upper-layer fluid pressure P_h^f imposed at the interface and the moving bottom boundary condition resulting from the time-varying landslide position and thickness, as well as the

friction between the slide and water. The upper-layer fluid pressure at the interface can be obtained by

$$P_h^f = \rho^f g(\eta + d) + Q_d, \tag{51}$$

where Q_d represents the contribution from the non-hydrostatic pressure.

Given the temporal variation of the bottom geometry, impermeability boundary conditions at the free-surface and bottom boundaries for the upper water layer are given by

$$w_\eta = \frac{\partial \eta}{\partial t} + u_\eta \frac{\partial \eta}{\partial x} + v_\eta \frac{\partial \eta}{\partial y}, \qquad w_d = -\frac{\partial d}{\partial t} - u_d \frac{\partial d}{\partial x} - v_d \frac{\partial d}{\partial y}, \tag{52}$$

where the subscripts 'η' and 'd' denote the boundary locations of free surface $|_{z=\eta}$ and the landslide-water interface $|_{z=-d}$, respectively.

Utilising (52) and integrating (45) over the water depth, we also obtain the equation for the free-surface elevation

$$\frac{\partial \eta}{\partial t} + \frac{\partial H\bar{u}}{\partial x} + \frac{\partial H\bar{v}}{\partial y} = -\frac{\partial d}{\partial t}, \tag{53}$$

where $\bar{u} = \int_0^1 u\, d\sigma$, $\bar{v} = \int_0^1 v\, d\sigma$, and $\frac{\partial d}{\partial t}$ can be computed via the temporal variation of landslide thickness.

2.4. List of assumptions

For clarity, the assumptions adopted for the mathematical formulation are summarized as follows:

- The inter-granular stresses are represented using Coulomb friction (specifically the Savage–Hutter formulation);
- The stresses inside the landslide increase linearly with landslide thickness;
- The landslide and surrounding water remain in contact, and shear stresses at the landslide-water interface are neglected;
- The granular quantities have contributions from both the solid and fluid phases, and both phases have the same velocity;
- The slide flow is incompressible, and the fluid phase is homogeneous with an isotropic stress.

3. Numerical formulation

3.1. Finite element discretisation

3.1.1. Function spaces

The model variables of the coupled two-layer system (39, 45–48, 53) are h, p, q for the lower landslide layer and η, u, v, w, Q for the upper wave flow layer. Choices of the function spaces for these variables are essential to the numerical stability and accuracy.

The discretisation in this paper for both landslide and free-surface flows is based on a linear discontinuous Galerkin function space, $\mathrm{P}_1^{\mathrm{DG}}$. The lower-layer granular landslide model solves depth-averaged equations based upon 2D triangular elements, and it is discretised using an equal order DG element pair for the landslide thickness h, the horizontal depth-averaged momentum components p and q. The computational domain Γ is divided into a finite set Γ_e of sub-domains, and based on Lagrangian basis functions

$\phi_i : E \subset \mathbb{R}^2 \to \mathbb{R}$, a piecewise polynomial function space $\mathbb{W}$ is defined upon the sub-domains. For $\mathrm{P}_1^{\mathrm{DG}}$discretisation, linear polynomials are assumed within triangles with no continuity enforced between adjacent elements. With appropriate Riemann fluxes embedded at element interfaces the $\mathrm{P}_1^{\mathrm{DG}}$element pair is well suited for shallow water problems [67, 76].

The upper-layer free-surface flow model uses 3D prismatic elements which are extruded from the same horizontal triangles that subdivide the horizontal domain Γ used in the lower-layer model. The 3D σ-coordinate domain Ω is divided into a finite set Ω_e of prisms, and the function space defined on Ω_e is the tensor product of the horizontal function space $\mathbb{W} = \mathrm{P}_1^{\mathrm{DG}}(\Gamma_e)$ and a vertical function space $\mathrm{P}_1^{\mathrm{DG}}(V_e)$, i.e. $\mathbb{V} = \mathrm{P}_1^{\mathrm{DG}}(\Gamma_e) \otimes \mathrm{P}_1^{\mathrm{DG}}(V_e)$. For more details of the finite element function spaces, readers may refer to [22, 47].

In order to facilitate the derivation of weak forms, we use the following shorthand notation

$$\left\langle \bullet \right\rangle_{\Gamma} = \sum_{E \in \Gamma_e} \int_E \bullet \, d\boldsymbol{x}_h, \qquad \left\langle\!\left\langle \bullet \right\rangle\!\right\rangle_{\mathcal{I}_\Gamma} = \sum_{I \in \mathcal{I}_\Gamma} \int_I \bullet \, dS,$$

$$\left\langle \bullet \right\rangle_{\Omega} = \sum_{E \in \Omega_e} \int_E \bullet \, d\boldsymbol{x}, \qquad \left\langle\!\left\langle \bullet \right\rangle\!\right\rangle_{\mathcal{I}_\Omega} = \sum_{I \in \mathcal{I}_\Omega} \int_I \bullet \, dA,$$

where $\langle \bullet \rangle$ represents the spatial integral over elements, while $\langle\langle \bullet \rangle\rangle$ denotes that over interfaces.

In addition, the notation $\{\bullet\} = (\bullet_L + \bullet_R)/2$ and $[[\bullet]] = (\bullet_L - \bullet_R)/2$ are adopted for mean and jump operator, respectively. To be specific,

$$\{a\} = \frac{1}{2}(a_L + a_R), \qquad \{\mathbf{u}\} = \frac{1}{2}(\mathbf{u}_L + \mathbf{u}_R), \qquad [[a\mathbf{n}]] = a_L\mathbf{n}_L + a_R\mathbf{n}_R,$$

where a and $\mathbf{u}$ represent scalar and vector fields, respectively. The subscripts 'L' and 'R' represents the cell interface's negative and positive side, respectively, and $\mathbf{n} = [n_x, n_y, n_z]$ denotes the outward unit normal vector.

3.1.2. Discretisation of the granular landslide model

Multiplying (39) by an test function $\boldsymbol{\phi}_h \in \mathbb{W} \times \mathbb{W} \times \mathbb{W}$, and integrating by parts over elements in the 2D domain Γ, the following weak form is obtained:

$$\left\langle \frac{\partial \mathbf{W}}{\partial t} \cdot \boldsymbol{\phi}_h \right\rangle_{\Gamma} + \left\langle\!\left\langle [[\hat{\mathbf{F}} \cdot \boldsymbol{\phi}_h]] \right\rangle\!\right\rangle_{\mathcal{I}_\Gamma} - \left\langle \mathbf{F} \cdot \nabla_h \boldsymbol{\phi}_h \right\rangle_{\Gamma} = \left\langle \mathbf{S} \cdot \boldsymbol{\phi}_h \right\rangle_{\Gamma}, \tag{54}$$

where $\hat{\mathbf{F}}$ denotes the numerical flux.

In the present work, a Harten–Lax–van Leer–Contact (HLLC) Riemann solver [72] is used to compute the numerical flux at cell faces. As an improvement to the classical Harten–Lax–van Leer (HLL) Riemann solver [77], HLLC is able to maintain the rarefaction wave and is thus preferred in resolving contact discontinuities. It should also be noted that other choices of Riemann solver are feasible, such as the Roe-type Riemann solver, a fairly common choice in industry standard flood modelling [78] and which has also previously been used for granular flow and landslide modelling [54, 79].

To compute fluxes of the variable vector $\mathbf{W}$, we consider the states to the left and to the right of the discontinuity, denoted by $\mathbf{W}_L$ and $\mathbf{W}_R$, respectively, as well as the averaged intermediate states $\mathbf{W}_L^*$ and $\mathbf{W}_R^*$. The four states are separated by three waves, whose speeds are denoted by S_L, S^* and S_R. The wave speeds are estimated by [80]

$$S_L = \min(\mathrm{v}_L - c_L,\ \mathrm{v}_R - c_R), \qquad S_R = \max(\mathrm{v}_L + c_L,\ \mathrm{v}_R + c_R), \tag{55}$$

$$S^* = \frac{\frac{1}{2}gh_L^2\cos^2\theta - \frac{1}{2}gh_R^2\cos^2\theta + h_R\mathrm{v}_R(S_R - \mathrm{v}_R) - h_L\mathrm{v}_L(S_L - \mathrm{v}_L)}{h_R(S_R - \mathrm{v}_R) - h_L(S_L - \mathrm{v}_L)}, \tag{56}$$

where $\mathrm{v} = \bar{\mathbf{v}}' \cdot \mathbf{n}_h'$ is the normal velocity at element facets in the local coordinate and c is the ideal gravity wave speed represented by $c = \sqrt{\Lambda_2 g h \cos^2\theta}$.

The approximate Riemann solution is defined as

$$\hat{\mathbf{W}} = \begin{cases} \mathbf{W}_L & \text{if } S_L > 0, \\ \mathbf{W}_L^* & \text{if } S_L \le 0 \le S^*, \\ \mathbf{W}_R^* & \text{if } S^* \le 0 \le S_R, \\ \mathbf{W}_R & \text{if } S_R < 0, \end{cases} \tag{57}$$

and the corresponding HLLC flux is given by

$$\hat{\mathbf{F}} = \begin{cases} \mathbf{n}_h' \cdot \mathbf{F}_L & \text{if } S_L > 0, \\ \mathbf{F}_L^*(\mathbf{W}_L, \mathbf{W}_R) & \text{if } S_L \le 0 \le S^*, \\ \mathbf{F}_R^*(\mathbf{W}_L, \mathbf{W}_R) & \text{if } S^* \le 0 \le S_R, \\ \mathbf{n}_h' \cdot \mathbf{F}_R & \text{if } S_R < 0. \end{cases} \tag{58}$$

There are various ways of estimating the intermediate states and flux $\mathbf{W}^*$ and $\mathbf{F}^*$, e.g. [77, 81, 82]. In this study, the HLLC flux is evaluated in the general form

$$\hat{\mathbf{F}} = \frac{1}{2}\Big[\mathbf{n}_h' \cdot (\mathbf{F}_L + \mathbf{F}_R) - (|S_L| - |S^*|)\,\mathbf{W}_L^* + (|S_R| - |S^*|)\,\mathbf{W}_R^* + |S_L|\mathbf{W}_L - |S_R|\mathbf{W}_R\Big] \tag{59}$$

with

$$\mathbf{W}_L^* = \frac{S_L - \mathrm{v}_L}{S_L - S^*}\Big(\mathbf{W}_L + [0,\ h_L \cos\theta (S^* - \mathrm{v}_L) n_x',\ h_L \cos\theta (S^* - \mathrm{v}_L) n_y']^T\Big), \tag{60}$$

$$\mathbf{W}_R^* = \frac{S_R - \mathrm{v}_R}{S_R - S^*}\Big(\mathbf{W}_R + [0,\ h_R \cos\theta (S^* - \mathrm{v}_R) n_x',\ h_R \cos\theta (S^* - \mathrm{v}_R) n_y']^T\Big), \tag{61}$$

where n_x' and n_y' denote components of the unit normal vector $\mathbf{n}_h'$ in the local coordinate system, and in the practical numerical implementation $\mathbf{n}_h'$ is implemented by the horizontal unit normal vector in the Cartesian coordinate, i.e. $\mathbf{n}_h' = [n_x, \frac{1}{\cos\theta} n_y]$.

3.1.3. Discretisation of the water wave model

To model the dispersive free-surface wave dynamics, we use the non-hydrostatic version of the 3D coastal ocean model *Thetis*, which adopts the DG-FE discretisation. Details of the discretisation may be found in [22, 47, 68], with essential components only briefly presented here.

In terms of the wave equations' solution, the momentum equations (46)–(48) are first solved without the dynamic pressure terms considered. The weak formulation is obtained by multiplying the momentum equations by arbitrary test functions $\psi_u \in \mathbb{V}$, $\psi_v \in \mathbb{V}$ and $\psi_w \in \mathbb{V}$, and performing integration over the σ-coordinate domain Ω, to

yield:

$$\left\langle \frac{\partial u}{\partial t}\psi_u \right\rangle_\Omega + \underbrace{\left\langle\left\langle u^{\mathrm{up}}\{u\}[[\psi_u n_x]]\right\rangle\right\rangle_{\mathcal{I}_\Omega} - \left\langle u\frac{\partial \psi_u u}{\partial x}\right\rangle_\Omega}_{\text{advection term } u\frac{\partial u}{\partial x}} + \underbrace{\left\langle\left\langle u^{\mathrm{up}}\{v\}[[\psi_u n_y]]\right\rangle\right\rangle_{\mathcal{I}_\Omega} - \left\langle u\frac{\partial \psi_u v}{\partial y}\right\rangle_\Omega}_{\text{advection term } v\frac{\partial u}{\partial y}}$$
$$+ \underbrace{\left\langle\left\langle u^{\mathrm{up}}\{\omega\}[[\psi_u n_\sigma]]\right\rangle\right\rangle_{\mathcal{I}_\Omega} - \left\langle u\frac{\partial \psi_u \omega}{\partial \sigma}\right\rangle_\Omega}_{\text{advection term } \omega\frac{\partial u}{\partial \sigma}} + \underbrace{\left\langle\left\langle g\{\eta\}[[\psi_u n_x]]\right\rangle\right\rangle_{\mathcal{I}_\Omega} - \left\langle g\eta\frac{\partial \psi_u}{\partial x}\right\rangle_\Omega}_{\text{elevation gradient term } g\frac{\partial \eta}{\partial x}} = 0, \tag{62}$$

$$\left\langle \frac{\partial v}{\partial t}\psi_v \right\rangle_\Omega + \underbrace{\left\langle\left\langle v^{\mathrm{up}}\{u\}[[\psi_v n_x]]\right\rangle\right\rangle_{\mathcal{I}_\Omega} - \left\langle v\frac{\partial \psi_v u}{\partial x}\right\rangle_\Omega}_{\text{advection term } u\frac{\partial v}{\partial x}} + \underbrace{\left\langle\left\langle v^{\mathrm{up}}\{v\}[[\psi_v n_y]]\right\rangle\right\rangle_{\mathcal{I}_\Omega} - \left\langle v\frac{\partial \psi_v v}{\partial y}\right\rangle_\Omega}_{\text{advection term } v\frac{\partial v}{\partial y}}$$
$$+ \underbrace{\left\langle\left\langle v^{\mathrm{up}}\{\omega\}[[\psi_v n_\sigma]]\right\rangle\right\rangle_{\mathcal{I}_\Omega} - \left\langle v\frac{\partial \psi_v \omega}{\partial \sigma}\right\rangle_\Omega}_{\text{advection term } \omega\frac{\partial v}{\partial \sigma}} + \underbrace{\left\langle\left\langle g\{\eta\}[[\psi_v n_y]]\right\rangle\right\rangle_{\mathcal{I}_\Omega} - \left\langle g\eta\frac{\partial \psi_v}{\partial y}\right\rangle_\Omega}_{\text{elevation gradient term } g\frac{\partial \eta}{\partial y}} = 0, \tag{63}$$

$$\left\langle \frac{\partial w}{\partial t}\psi_w \right\rangle_\Omega + \underbrace{\left\langle\left\langle w^{\mathrm{up}}\{u\}[[\psi_w n_x]]\right\rangle\right\rangle_{\mathcal{I}_\Omega} - \left\langle w\frac{\partial \psi_w u}{\partial x}\right\rangle_\Omega}_{\text{advection term } u\frac{\partial w}{\partial x}} + \underbrace{\left\langle\left\langle w^{\mathrm{up}}\{v\}[[\psi_w n_y]]\right\rangle\right\rangle_{\mathcal{I}_\Omega} - \left\langle w\frac{\partial \psi_w v}{\partial y}\right\rangle_\Omega}_{\text{advection term } v\frac{\partial w}{\partial y}}$$
$$+ \underbrace{\left\langle\left\langle w^{\mathrm{up}}\{\omega\}[[\psi_w n_\sigma]]\right\rangle\right\rangle_{\mathcal{I}_\Omega} - \left\langle w\frac{\partial \psi_w \omega}{\partial \sigma}\right\rangle_\Omega}_{\text{advection term } \omega\frac{\partial w}{\partial \sigma}} = 0, \tag{64}$$

where the superscript 'up' represents the conventional upwind value at the cell interfaces, and boundary condition terms have been omitted for simplicity.

The velocities u, v, w solved for based upon the weak forms (62)–(64) are intermediate and need to be substituted into the mass equation (45) to yield the 3D Poisson equation for the non-hydrostatic pressure Q (see Eq. (61) in [47]). Its weak formulation has been presented in Eq. (68) in [47] and are not repeated here for brevity. However, note that in this study due to the moving bottom boundary from landslide motion, another boundary term should be added to the right-hand side of the original weak form of the Poisson equation to account for the coupling dynamics, which is given by

$$\left\langle\left\langle \frac{\rho^f}{\Delta t}\frac{1}{H}\left(\frac{h^{n+1}-h^n}{\Delta t}\right)_{\mathrm{3d}} n_z \psi_q \right\rangle\right\rangle_{\partial\Omega_b}, \tag{65}$$

where ψ_q is the test function for Q, and $\partial\Omega_b$ denotes the bottom boundary of the domain Ω. The superscript '$n+1$' and 'n' represent the current and previous time step levels and the time step size is $\Delta t = t^{n+1} - t^n$. The subscript '3d' implies that it is a 3D field from the vertical extrusion of the 2D landslide thickness h.

Given the corrected velocity fields, the surface elevation should be updated accordingly by solving the depth-integrated equation (53). The weak form reads

$$\left\langle \frac{\partial \eta}{\partial t}\phi_\eta \right\rangle_\Gamma + \left\langle\left\langle \{H\}\bar{u}^*[[\phi_\eta n_x]]\right\rangle\right\rangle_{\mathcal{I}_\Gamma} - \left\langle H\bar{u}\frac{\partial \phi_\eta}{\partial x}\right\rangle_\Gamma$$
$$+ \left\langle\left\langle \{H\}\bar{v}^*[[\phi_\eta n_y]]\right\rangle\right\rangle_{\mathcal{I}_\Gamma} - \left\langle H\bar{v}\frac{\partial \phi_\eta}{\partial y}\right\rangle_\Gamma = \left\langle \frac{\partial h}{\partial t}\phi_\eta \right\rangle_\Gamma, \tag{66}$$

where $\phi_\eta \in \mathbb{W}$ is the test function, and the linear Roe solution [76] gives $\bar{u}^* = \{\bar{u}\} + \sqrt{g/\{H\}}[[\eta n_x]]$ and $\bar{v}^* = \{\bar{v}\} + \sqrt{g/\{H\}}[[\eta n_y]]$. Note that the right-hand side term stands for the temporal variation of landslide thickness, and the total depth of the upper-layer water H also accounts for the effect of the landslide thickness h.

3.2. Coupled time integration scheme

For time stepping of the coupled two-layer system, a two-stage time integration scheme is used. For convenience we rewrite the lower-layer landslide equation (39) and the upper-layer water wave equations (46)–(48) as

$$\frac{\partial \mathbf{W}}{\partial t} = \mathcal{F}(\theta, \mathbf{W}) + \mathcal{S}(\mathbf{W}, P_h^f), \tag{67}$$

$$\frac{\partial \mathbf{U}}{\partial t} = \mathcal{A}(\mathbf{U}, \mathbf{W}) + \mathcal{P}(Q, h), \tag{68}$$

where $\mathbf{U} = [u, v, w]^T$ denotes the 3D velocity of the upper-layer water and $\mathcal{A}$ denotes terms treated explicitly, such as advection and 3D elevation gradient terms. P_h^f in $\mathcal{S}$ consists of contributions from the non-hydrostatic pressure Q and free-surface elevation η appearing in (68), while $\mathbf{W}$ included in $\mathcal{A}$ is to account for the inter-layer friction and the landslide motion (67) acting on the upper-layer domain with the moving bottom boundary condition.

We use a second-order Strong Stability Preserving Runge–Kutta scheme, SSPRK(2,2) [83] to advance (67)–(68) in time. For a generic problem $\frac{\partial c}{\partial t} = F(c)$, the scheme reads

$$c^{(1)} = c^n + \Delta t F(c^n), \qquad c^{(2)} = c^{(1)} + \Delta t F(c^{(1)}) \tag{69}$$

$$c^{n+1} = \frac{1}{2}c^n + \frac{1}{2}c^{(2)} = c^n + \frac{1}{2}\Delta t F(c^n) + \frac{1}{2}\Delta t F(c^{(1)}). \tag{70}$$

The first stage of time stepping evaluates the intermediate level of both the landslide and water velocity variables:

$$\left\langle \mathbf{W}^{(1)} \cdot \boldsymbol{\phi}_h \right\rangle_\Gamma = \left\langle \mathbf{W}^n \cdot \boldsymbol{\phi}_h \right\rangle_\Gamma + \Delta t \left\langle \Big(\mathcal{F}(\theta, \mathbf{W}^n) + \mathcal{S}(\mathbf{W}^n, Q^n, \eta^n) \Big) \cdot \boldsymbol{\phi}_h \right\rangle_\Gamma, \tag{71}$$

$$\left\langle \mathbf{U}^* \cdot \boldsymbol{\psi}_{\boldsymbol{u}} \right\rangle_{\Omega^{(1)}} = \left\langle \mathbf{U}^n \cdot \boldsymbol{\psi}_{\boldsymbol{u}} \right\rangle_{\Omega^n} + \Delta t \left\langle \mathcal{A}(\mathbf{U}^n, \mathbf{W}^{(1)}, \eta^{(1)}) \cdot \boldsymbol{\psi}_{\boldsymbol{u}} \right\rangle_{\Omega^n}, \tag{72}$$

$$\left\langle \mathbf{U}^{(1)} \cdot \boldsymbol{\psi}_{\boldsymbol{u}} \right\rangle_{\Omega^{(1)}} = \left\langle \mathbf{U}^* \cdot \boldsymbol{\psi}_{\boldsymbol{u}} \right\rangle_{\Omega^{(1)}} + \Delta t \left\langle \mathcal{P}(Q^{(1)}, h^{(1)}) \cdot \boldsymbol{\psi}_{\boldsymbol{u}} \right\rangle_{\Omega^{(1)}}, \tag{73}$$

where the pressure projection method is adopted to solve for the non-hydrostatic pressure $Q^{(1)}$, i.e. substituting (73) into the continuity equation (45) and solving the resulting Poisson equation for $Q^{(1)}$ (see Eq. (61) and (68) in [47]). With the value of $Q^{(1)}$, the velocity $\mathbf{U}^{(1)}$ is updated via (73). The whole time stepping is based on a fixed computational domain, and the domain notations $\Omega^{(1)}$, Ω^n (with the superscripts $^{(1)}$ and ^{n} denoting time step levels) actually represent the time-varying physical domain with respect to the free-surface perturbation and the moving bottom boundary. In the numerical implementation, they are represented by the σ-transformation terms (49)–(50) computed at each stage.

Similarly, the second stage advances the coupled equations in time as follows:

$$\left\langle \mathbf{W}^{n+1}\cdot\boldsymbol{\phi}_h\right\rangle_\Gamma = \left\langle \mathbf{W}^{n}\cdot\boldsymbol{\phi}_h\right\rangle_\Gamma + \frac{1}{2}\Delta t\left\langle \Big(\mathcal{F}(\theta,\mathbf{W}^n)+\mathcal{S}(\mathbf{W}^n,Q^n,\eta^n)\Big)\cdot\boldsymbol{\phi}_h\right\rangle_\Gamma + \frac{1}{2}\Delta t\left\langle \Big(\mathcal{F}(\theta,\mathbf{W}^{(1)})+\mathcal{S}(\mathbf{W}^{(1)},Q^{(1)},\eta^{(1)})\Big)\cdot\boldsymbol{\phi}_h\right\rangle_\Gamma \tag{74}$$

$$\left\langle \mathbf{U}^{*}\cdot\boldsymbol{\psi}_{\boldsymbol{u}}\right\rangle_{\Omega^{(2)}} = \left\langle \mathbf{U}^{(1)}\cdot\boldsymbol{\psi}_{\boldsymbol{u}}\right\rangle_{\Omega^{(1)}} + \Delta t\left\langle \mathcal{A}(\mathbf{U}^{(1)},\mathbf{W}^{n+1},\eta^{(2)})\cdot\boldsymbol{\psi}_{\boldsymbol{u}}\right\rangle_{\Omega^{(1)}}, \tag{75}$$

$$\left\langle \mathbf{U}^{(2)}\cdot\boldsymbol{\psi}_{\boldsymbol{u}}\right\rangle_{\Omega^{(2)}} = \left\langle \mathbf{U}^{*}\cdot\boldsymbol{\psi}_{\boldsymbol{u}}\right\rangle_{\Omega^{(2)}} + \Delta t\left\langle \mathcal{P}(Q^{(2)},h^{n+1})\cdot\boldsymbol{\psi}_{\boldsymbol{u}}\right\rangle_{\Omega^{(2)}}, \tag{76}$$

where the final values of the landslide variables are obtained which are subsequently used for the wave flow equations. The pressure projection is again used in the same way as the first stage and the velocity is corrected with the substitution of non-hydrostatic pressure $Q^{(2)}$ into (76). The final velocity can then be obtained based on $\mathbf{U}^{n+1} = \frac{1}{2}\mathbf{U}^n + \frac{1}{2}\mathbf{U}^{(2)}$.

Along with the time advancing of the coupled system, the free-surface elevation (53) is also advanced with a compatible two-stage time integration scheme [67]:

$$c^{(1)} = c^n + \Delta t F(c^n), \tag{77}$$

$$c^{n+1} = c^n + \frac{1}{2}\Delta t F(c^n) + \frac{1}{2}\Delta t F(c^{n+1}), \tag{78}$$

which is a combination of a forward Euler and trapezoidal steps. Denoting the weak form of the divergence term in the free-surface equation (66) by $\mathcal{G}$, the two-stage time stepping for the elevation in (71)–(76) is given as follows

$$\left\langle \eta^{(1)}\phi_\eta\right\rangle_\Gamma = \left\langle \eta^{n}\phi_\eta\right\rangle_\Gamma + \Delta t\left\langle \mathcal{G}(\eta^n,\bar{u}^n,\bar{v}^n)\phi_\eta\right\rangle_\Gamma, \tag{79}$$

$$\left\langle \eta^{(2)}\phi_\eta\right\rangle_\Gamma = \left\langle \eta^{n}\phi_\eta\right\rangle_\Gamma + \frac{1}{2}\Delta t\left\langle \Big(\mathcal{G}(\eta^n,\bar{u}^n,\bar{v}^n)+\mathcal{G}(\eta^{(2)},\bar{u}^{(1)},\bar{v}^{(1)})\Big)\phi_\eta\right\rangle_\Gamma. \tag{80}$$

To be specific, the elevations $\eta^{(1)}$ and $\eta^{(2)}$ are updated first at each stage before advancing the 3D momentum of upper layer water, i.e. (72) and (75). Once the landslide thickness and position as well as the upper-layer surface elevation are known, it is straightforward to compute the σ-transformation terms (49)–(50) which actually originate from the movement of the physical domain. Based on the underlying practical physical domain, e.g. denoting $\Omega^{(1)}$ and $\Omega^{(2)}$ at different stages, the momentum equations can be advanced accurately. It is also noted that using the divergence-free velocity field $\mathbf{U}^{n+1}$ the final free-surface elevation η^{n+1} can be obtained via (53), leading to the updated domain Ω^{n+1} and associated σ-transformation terms for the next time step.

In terms of choosing the time step, the stability of the coupled two-layer system constrains the maximal admissible time step. According to the Courant-Friedrichs–Lewy (CFL) condition, the typical admissible time step is [84]

$$\Delta t \propto \frac{L}{c+U}, \tag{81}$$

where L denotes the length scale of an element, which is taken as the square root of area of the triangle element for horizontal domain. $U \geq 0$ is the maximal advective speed. c is the speed of the surface gravity waves, and $c = \sqrt{\Lambda_2 gh\cos^2\theta}$ and $c = \sqrt{gH}$ are used for the lower and upper layer, respectively. It is naturally noted that the maximal admissible time step for the lower- and upper-layer time advancing may not match. Our preliminary experiments indicated that the maximal admissible time step size for the lower layer is generally lower than that for the upper layer. It is to some extent explained that the

length scale of the landslide is much smaller than that of the water wave, which results in the smaller time step size required.

As the computational cost of the upper-layer 3D model, with solving the Poisson equation for the non-hydrostatic pressure, is significantly higher, for the sake of computational efficiency of the coupled model the lower-layer granular flow is set to be solved with a higher temporal resolution satisfying (81), i.e. $\delta t = \Delta t/M$, where M is the integer time step ratio, and with an time index $m \in [0, M]$ the corresponding time is $t^m = t^n + m\delta t$. The presentation of (71) and (74) adopts the time step with a specific case of $M = 1$. For a general and complete solution procedure, the whole time integration scheme is summarised in Algorithm 1.

Algorithm 1: Summary of the coupled time integration scheme

Input: Model variables at time t^n: $\mathbf{W}^n, \mathbf{U}^n, \eta^n, Q^n$
Output: Model variables at time t^{n+1}: $\mathbf{W}^{n+1}, \mathbf{U}^{n+1}, \eta^{n+1}, Q^{n+1}$
$t^m \leftarrow t^n$;
while $t^m \leq t^{n+1}$ **do**
  First stage:
  1: Solve 2D lower-layer granular flow for $\mathbf{W}^{(1)}$, i.e. ($h^{(1)}$, $p^{(1)}$, $q^{(1)}$) (71);
  2: Apply wetting and drying treatments for $\mathbf{W}^{(1)}$ (82)–(87);
  if $t^m = t^{n+1}$ **then**
    3: Update bathymetry $d^{(1)}$ and expand $d^{(1)}$, $h^{(1)}$ to the 3D fields $d_{3\mathrm{d}}^{(1)}$, $h_{3\mathrm{d}}^{(1)}$;
    4: Compute the temporal variation of slide thickness and update free-surface elevation $\eta^{(1)}$ (79);
    5: Compute σ-coordinate based vertical velocity $\omega^{(1)}$ (50);
    6: Update the non-hydrostatic pressure $Q^{(1)}$ and 3D upper-layer momentum equations for $\mathbf{U}^{(1)}$, i.e. ($u^{(1)}$, $v^{(1)}$, $w^{(1)}$) (72)–(73);
    7: Extract the non-hydrostatic pressure at the landslide-water interface from $Q^{(1)}$, and compute the total upper-layer fluid pressure P_h^f (51);
  end
  Second stage:
  8: Solve 2D lower-layer granular flow for $\mathbf{W}^m$ (74);
  9: Apply wetting and drying treatments for $\mathbf{W}^m$ (82)–(87);
  if $t^m = t^{n+1}$ **then**
    10: Update bathymetry d^{n+1} and expand d^{n+1}, h^{n+1} to the 3D fields $d_{3\mathrm{d}}^{n+1}$, $h_{3\mathrm{d}}^{n+1}$;
    11: Compute the temporal variation of slide thickness and update free-surface elevation $\eta^{(2)}$ (80);
    12: Compute σ-coordinate based vertical velocity $\omega^{(2)}$ (50);
    13: Update the non-hydrostatic pressure $Q^{(2)}$ and 3D upper-layer momentum equations for divergence-free velocity $\mathbf{U}^{n+1}$ (75)–(76);
    14: Extract the non-hydrostatic pressure at the landslide-water interface from $Q^{(2)}$, and compute the total upper-layer fluid pressure P_h^f (51);
    15: Update the final free-surface elevation η^{n+1} and ω^{n+1};
  end
  $t^m \leftarrow t^m + \delta t$;
end

3.3. Wetting and drying treatments

In the modelling of granular subaerial landslides and wave generation, wetting and drying (WD) processes are expected to occur both in terms of the landslide movement

across the dry bed, and also with regards to the resulting free-surface waves forming a wet-dry interface moving across the landslide or the non-erodible bottom (e.g. in modelling phenomena such as wave run-up and run-down). To treat the wetting and drying properly, two different WD techniques are adopted in this work for the lower-layer landslide and upper-layer free-surface flows, respectively.

3.3.1. Wetting and drying treatment for landslide model

For slide collapse and flow across the dry bed, a classical thin-layer technique is implemented in the model based on a fixed mesh (as opposed to a mesh that moves with the slide). It is relatively straightforward to use this technique with a FV approach [85–87] by first detecting the dry cells below a depth threshold ϵ and properly determining the flux at dry cell interfaces. For DG-FE, however, a different treatment is needed to ensure positivity of the mean depth within each finite element and a well-balanced numerical flux computation is used to limit numerical oscillations and preserve steady states at rest.

The present numerical implementation closely follows the method presented by [70], in which the nodal depth h_i and momentum $\boldsymbol{m}_i$ within an element are modified element-wise. The basic treatment is as follows:

(1) If $h_i \geq \epsilon$, $\forall i \in \{1,2,3\}$, then

$$\tilde{h}_i = h_i, \ \forall i \in \{1,2,3\}. \tag{82}$$

(2) If $\bar{h} \leq \epsilon$, then

$$\tilde{h}_i = \bar{h}, \ \forall i \in \{1,2,3\}. \tag{83}$$

(3) If $\bar{h} > \epsilon$, sort the values of h_i in ascending order, leading to $h_{n_1} \leq h_{n_2} \leq h_{n_3}$, then

$$\tilde{h}_{n_1} = \epsilon, \tag{84}$$

$$\tilde{h}_{n_2} = \max(\epsilon, h_{n_2} - (\tilde{h}_{n_1} - h_{n_1})/2), \tag{85}$$

$$\tilde{h}_{n_3} = h_{n_3} - (\tilde{h}_{n_1} - h_{n_1}) - (\tilde{h}_{n_2} - h_{n_2}). \tag{86}$$

(4) Remove the momentum at dry nodes and evenly distribute to wet nodes

$$\tilde{\boldsymbol{m}}_i = \alpha_i \left(\boldsymbol{m}_i + \Delta\boldsymbol{m}/n_w\right), \tag{87}$$

where the procedure is applied at each Runge–Kutta time stepping stage. $\bar{h}$ denotes the average depth within an element, and $\tilde{h}_i$ and $\tilde{\boldsymbol{m}}_i$ denote the approximated nodal depth and momentum, respectively. $\alpha_i = \chi(\tilde{h}_i - \epsilon)$ is the flag denoting the wet or dry status of node i after modifying the depth, $n_w = \sum_{i=1}^{3} \alpha_i$ is the number of wet nodes, and $\Delta\boldsymbol{m} = \sum_{i=1}^{3} \boldsymbol{m}_i(1-\alpha_i)$ represents the sum of momentum at dry nodes. $\chi(\bullet)$ is the unit indicator function defined as that if $h \leq 0$, $\chi(h) = 0$ and else $\chi(h) = 1$. A detailed discussion of the method can be found in [70], and for brevity only essential components are presented here. In the present landslide model which includes a bed curvature variable (i.e. θ), we take the additional step, as in [79], to not consider bed curvature around the WD interface for calculating the numerical fluxes, which can prevent potential issues associated with artificial numerical waves caused by the bed curvature changes and further ensure the steady state solution of the model.

3.3.2. Wetting and drying treatment for water wave model

The thin-layer WD method used in the lower-layer landslide modelling relies on explicit detection of dry elements, and the time step size is strictly constrained by the WD front which can propagate only by one element per time step [88]. The resulting explicit time integration scheme required would lead to significantly growing computational cost

for the upper-layer 3D non-hydrostatic simulations with relatively high vertical mesh resolution. In addition, the thin-layer WD approach is generally aimed at conserving numerical mass only, which is sufficient for the gradually propagating granular (landslide) flow; in terms of the dynamic landslide-water interaction, however, the potential artificial pressure gradient problem may lead to serious momentum conservation issues and further affect the accuracy of the coupled two-layer modelling.

To represent the complex moving shoreline with respect to the landslide-generated waves interacting with the uneven bottom or the landslide interface (taking account of the additional slide thickness over the original non-erodible bottom), a different implicit wetting and drying method [47, 88] is applied in this work to naturally circumvent the artificial pressure gradient problem. The underlying idea is to choose an appropriate modification function $f(H)$ of the total water depth H to ensure $\widetilde{H} = H + f(H) \geq 0$ in the whole domain. Note that the free surface level solved for can freely move below the dry area of bottom, although the total water depth actually "acknowledged" by the primitive equations is still positive with a spatially varying thin layer over the bed in drying phase. The advantages of this WD method include (a) no spurious free surface slope, (b) a smooth transition around the WD interface (or front), (c) the modification function can be naturally retained in both the primitive mass and momentum equations, and (d) the resulting feasible implicit time integration can reduce the computational cost.

Different modification functions are selected by [88] and [47], but the basis is the same. In this study we follow [47] and use

$$f(H) = \frac{2\delta^2}{2\delta + |H|} + \frac{1}{2}(|H| - H), \tag{88}$$

so that the redefined water depth is given by

$$\widetilde{H} = H + f(H) = \frac{2\delta^2}{2\delta + |H|} + \frac{1}{2}(|H| + H), \tag{89}$$

where H is a 2D field, and the parameter δ denoting the depth threshold at the WD interface (i.e. $H = 0$) is used to control the transition smoothness, which can affect the numerical stability significantly. It may be noticed that the modified water depth $\tilde{H}$ over the dry bed (i.e. where $H < 0$) is always positive, since the first term $\frac{2\delta^2}{2\delta+|H|} > 0$ and the latter term $\frac{1}{2}(|H| + H) = 0$ are satisfied unconditionally. In terms of the bed in the wetting phase, the modification (88) should be significant only near the WD front due to $f(H) = \frac{2\delta^2}{2\delta+H} \approx 0$ for large H.

Replacing H by $\widetilde{H}$, the weak formulation of (66) is modified as

$$\begin{aligned}\left\langle \frac{\partial \eta}{\partial t}\phi_\eta \right\rangle_\Gamma + \left\langle \left\langle \{\widetilde{H}\}\bar{u}^*[[\phi_\eta n_x]] \right\rangle \right\rangle_{\mathcal{I}_\Gamma} - \left\langle \widetilde{H}\bar{u}\frac{\partial \phi_\eta}{\partial x} \right\rangle_\Gamma \\ + \left\langle \left\langle \{\widetilde{H}\}\bar{v}^*[[\phi_\eta n_y]] \right\rangle \right\rangle_{\mathcal{I}_\Gamma} - \left\langle \widetilde{H}\bar{v}\frac{\partial \phi_\eta}{\partial y} \right\rangle_\Gamma = \left\langle \frac{\partial h}{\partial t}\phi_\eta \right\rangle_\Gamma - \left\langle \frac{\partial f(H)}{\partial t}\phi_\eta \right\rangle_\Gamma .\end{aligned} \tag{90}$$

After updating the approximated 2D free-surface elevation and the still water depth including the slide thickness, the corresponding 3D fields $\eta_{3\mathrm{d}}$ and $d_{3\mathrm{d}}$ can be obtained from vertical extrusions.

To compute the 3D σ-transformation terms (49)–(50), the 3D water depth field (i.e.$H_{3\mathrm{d}} = \eta_{3\mathrm{d}} + d_{3\mathrm{d}}$) should also be adjusted in a similar manner as (89):

$$\widetilde{H}_{3\mathrm{d}} = \frac{2\delta^2}{2\delta + |H_{3\mathrm{d}}|} + \frac{1}{2}(|H_{3\mathrm{d}}| + H_{3\mathrm{d}}), \tag{91}$$

which is used to obtain the recovered vertical coordinate z^* in the Cartesian coordinate via $z^* = \sigma\widetilde{H}_{3\mathrm{d}} - d_{3\mathrm{d}}$, $\sigma \in [0,1]$. The σ-coordinate transformation terms, including ω, $\frac{\partial z^*}{\partial t}$, $\frac{\partial z^*}{\partial x}$, $\frac{\partial z^*}{\partial y}$ and $\frac{\partial \sigma}{\partial z^*} = \frac{1}{\widetilde{H}_{3\mathrm{d}}}$, are calculated using z^*. These terms are then employed in both advancing the momentum equations and solving the Poisson equation for the non-hydrostatic pressure.

4. Test cases

The coupled two-layer granular and free-surface flow model presented above is verified and validated in this section using a suite of test cases. The first three cases involve the validation of the granular landslide model. Among these, the model's capability of preserving the stationary solutions is first verified, and then a frictional dam break flow on a flat slope as well as a granular flow onto a sloped bed with curvature are considered to benchmark the accuracy of the granular model in representing wetting and drying transitions, friction and curvature effects. The subsequent cases with experimental measurements are adopted for examining the impulsive wave generation by subaerial landslides which involves both the lower- and upper-layer flows. Given the last two test cases also considered by [20], we compare our results against theirs.

4.1. Stationary solutions

In terms of the stationary solution, the granular material is considered with no movement, i.e. $\bar{v}_{x'} = \bar{v}_{y'} = 0$. Given this condition, the x–direction momentum equation in (39) gives

$$\frac{\partial \frac{1}{2}\Lambda_2 g h^2 \cos^3\theta}{\partial x} = -gh\cos\theta\frac{\partial b}{\partial x} - \frac{1}{4}gh^2\cos\theta\frac{\partial \cos^2\theta}{\partial x} + S_{\tau x}, \tag{92}$$

where for brevity the inter-layer coupling terms are not considered. According to [52], the coulomb friction term $S_{\tau x}$ can be understood by the fact that when the friction is lower than the basal critical stress (i.e. $|S_{\tau x}| < \sigma_c$), the granular landslide stops moving (i.e. $\bar{v}_{x'} = 0$), where $\sigma_c = (1 - r\lambda_2)gh\cos\theta\tan\phi_c$ with ϕ_c denoting the angle of repose of the sliding mass. We use this treatment in the practical numerical implementation to enforce zero velocity when the granular material is expected to stop moving. The following relation can be derived

$$\begin{aligned} |S_{\tau x}| &= \left| gh\cos\theta\frac{\partial b}{\partial x} + \frac{\partial \frac{1}{2}\Lambda_2 g h^2\cos^3\theta}{\partial x} + \frac{1}{4}gh^2\cos\theta\frac{\partial\cos^2\theta}{\partial x}\right| \\ &= \left| gh\cos\theta\frac{\partial b}{\partial x} + \Lambda_2 gh\frac{\partial h}{\partial x}\cos^3\theta + \frac{3\Lambda_2+1}{4}gh^2\cos\theta\frac{\partial\cos^2\theta}{\partial x}\right| < \sigma_c, \end{aligned} \tag{93}$$

i.e.

$$\left|\frac{\partial b}{\partial x} + \Lambda_2\frac{\partial h}{\partial x}\cos^2\theta + \frac{3\Lambda_2+1}{4}h\frac{\partial\cos^2\theta}{\partial x}\right| < (1 - r\lambda_2)\tan\phi_c \le \tan\phi_c. \tag{94}$$

Treating this relation as an equality, i.e. assuming the friction equals the critical stress, it forms a first order differential equation that can be solved for h with appropriate boundary conditions [79]. The inequality implies that the stationary flow surface is dependent of the values of Λ_2 and the bed curvature. When $\Lambda_2 = 1$, (94) reduces to $\left|\frac{\partial(b+h\cos^2\theta)}{\partial x}\right| < \tan\phi_c$; if further assuming the landslide material is in fact water, i.e. $\phi_b = \phi_c = 0$, the stationary solution becomes $b + h\cos^2\theta = \mathrm{cst}$.

To evaluate the model's ability to preserve the stationary solution discussed above, a simple numerical test is performed. An arc-shaped bottom with 1 m radius is adopted

to account for both the bed slope and curvature, with the geometry and the initial flow surface given by

$$b(x) = 1 - \sqrt{1-(x-1)^2}, \quad h(x) = \begin{cases} 0 & \text{if } b(x) \geq 0.235, \\ 0.235 - b(x) & \text{if } b(x) < 0.235. \end{cases} \tag{95}$$

In the numerical simulation, the domain is discretised with a split-quad mesh using 200 triangles, where a 2D (quasi 1D) computational domain with a single cell in the y-direction is in fact adopted in the simulation, i.e. $\Delta x = \Delta x = 0.01$m. The time step size is set as 0.001 s, and all boundaries are closed. A layer of still water is first considered with specifying zero friction angles (i.e. $k_{a/p} = \Lambda_2 = 1$). The numerical results are demonstrated in Fig. 2, and the left panel shows the artificial wave fluctuation (blue dashed line) caused by the bed curvature term (41) near the wetting and drying front. With the additional treatment as that in [79], i.e. the bed curvature is not considered in determining the numerical fluxes around the wetting and drying front, the present model can be ensured well-balanced and the steady state solution (red line) can be preserved as shown in Fig. 2(a).

Fig. 2(b) illustrates the final stationary profiles of three granular masses corresponding to $\Lambda_2 = 1.3$, 1.5 and 2.0 based on the same basal friction angle $\phi_b = 30°$. Not accounting for the upper-layer effects, Λ_2 is equal to $k_{a/p}$ and is dependent on the internal friction angle ϕ_i as indicated by (28), where $k_{a/p} = 1+\tan^2\phi_i$ can be derived if $k_{a/p} = (k_{act}+k_{pas})/2$ is considered for stationary solutions with zero velocities [52]. As shown by the inequality (94), the stable state is associated with the bed slope and curvature as well as the internal and basal friction angles. The higher value of Λ_2 means increasing internal friction angles and can result in (94) not being satisfied using the same initial conditions. In other words, the profile of the granular mass will keep moving until transitioning to a new stable state with a spatially varying $\frac{\partial h}{\partial x}$ and h. After reaching the new stable state, i.e. the inequality (94) has been satisfied, there will be no further movement of the granular mass and the surface profile will be preserved. This can be observed in Fig. 2(b) and it is clear that the final surface height of the granular flow and its gradient are different from those at initial position.

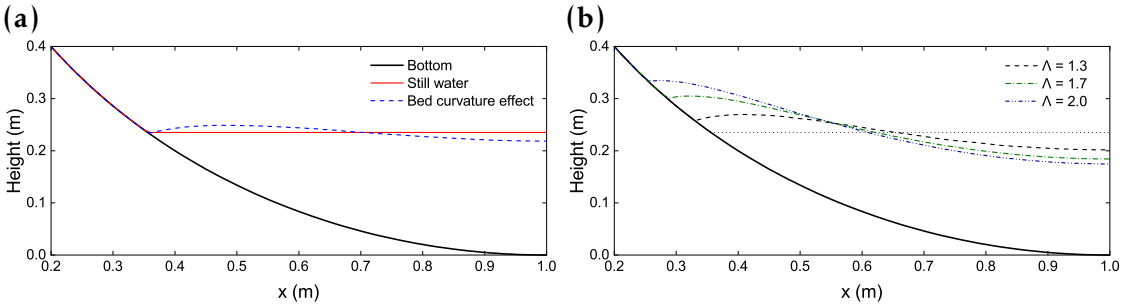


Figure 2: Numerical results corresponding to a layer of (a) water and (b) granular fluid at rest. Left panel (a): water with zero internal and basal friction, i.e. $\phi_i = \phi_b = 0°$ and $k_{a/p} = \Lambda_2 = 1$; (b) granular stationary surface with $\phi_b = 30°$ against different values of Λ_2 (i.e. the earth pressure coefficient $k_{a/p}$ for full dry granular flow without water mixed). The artificial wave caused by the bed curvature term in wetting and drying front is visualised by the blue dash line in panel (a).

4.2. Frictional dam break on a flat slope

To confirm the validity of the granular model implementation, a frictional dam break case which possesses an analytical solution [89] is used. The problem contains a discontinuity at the moving wetting and drying interface and thus the resulting dry bed Riemann

problem should be resolved properly. The analytical solution for the debris flow height as a function of space and time is given by

$$h_s(x,t) = \frac{1}{9g\cos\alpha}\left(\frac{x}{t} - 2c_0 + \frac{1}{2}mt\right)^2, \tag{96}$$

where $x = 0$ coincides with the initial front of the dam, α is the constant bed slope angle, $c_0 = \sqrt{gh_0\cos\alpha}$ is the wave celerity, h_0 is the initial dam height, and $m = -g\sin\alpha + g\cos\alpha\tan\phi_b$. This solution is only valid for the confined region $x_L < x < x_R$, where $x_L = -c_0t - \frac{1}{2}mt^2$ and $x_R = 2c_0t - \frac{1}{2}mt^2$, with the wider solution assumed flat outside.

The computational domain has a length of 2 km, and its left-hand side is occupied initially by the granular material with height $h_0 = 20$ m. With a split-quad mesh, the domain is discretised using 1000 triangles, in which the edge length of elements is 4 m and there is only a single element in the y-direction. The total simulation period is 15 s, and the time step size is 0.02 s. Except for the right-hand outflow boundary, all other boundaries are closed. The earth pressure coefficient $k_{a/p}$ is set to be unity, and the parameter λ_1 is set as zero corresponding to the isolation of the pore fluid from the upper water layer. λ_2 which is generally calibrated through laboratory measurements is here directly set to zero which is consistent with the dry granular flow based analytical solution. The wetting and drying depth threshold ϵ is set at 10^{-5} m.

Fig. 3 compares the simulated and analytical dam break profiles at time $t = 15$ s for the three cases with/without bed slope or bed friction. Specifically the first case is dam-break flow on a horizontal plane without basal friction, while the other two consider a bed slope angle of 20° in which the basal friction angles are 0° and 20°, respectively. For all three cases, the numerical results agree well with the exact solutions and the corresponding L_2 errors computed at the end of the simulations are 2.29%, 2.22% and 2.14%, respectively. This indicates that the implemented model can correctly simulate granular flow with a wetting and drying discontinuity.

4.3. Granular flow on a slope with bed curvature

The previous test case considers the dam break flow from an inclined slope onto a frictional flat bed with a constant slope angle. In this section, the experiments of [90] are adopted to assess the granular model's capability in representing the frictional flow on a bed with curvature. The experiments were performed in a 0.1 m wide chute which is made up of an inclined and a horizontal section (using a curved segment to connect and control the angle of inclination 40–60°). A finite mass of granular material is released down the inclined slope, passing the curved portion of the chute and depositing on the horizontal section. In the experiments, a series of inclination angles, mass weight, friction angles and earth pressure coefficient were tested; the current numerical study for model validation only considers experiment No. 113, in which the plastic grains with bulk density $\rho_g = 450\,\mathrm{kg/m^3}$ are released onto a slope with an inclination angle of 60 ° and the curved transition of 0.246 m radius, and the internal angle of friction, ϕ_i, and a bed friction angle, ϕ_b, are 29° and 23°, respectively.

The horizontal computational domain is 3.5 m, which is discretised using 700 triangles with only one element in the y-direction ($\Delta x = \Delta y = 0.1m$). The time step size is chosen as 0.0005 s, and the period of simulation is 2 s. The boundary is closed, and the wetting and drying depth threshold ϵ is set at 10^{-5} m. For the fully dry granular flow considered in this case, the parameters λ_1 and λ_2 are both set at zero. Dynamic internal friction angles are smaller than their static counterparts [90, 91], and it is feasible in ensuing computations to somewhat reduce the angle of internal friction from its measured value as that in [90]. We here adopt the internal angle of friction $\phi_i = 20°$ in the computation.

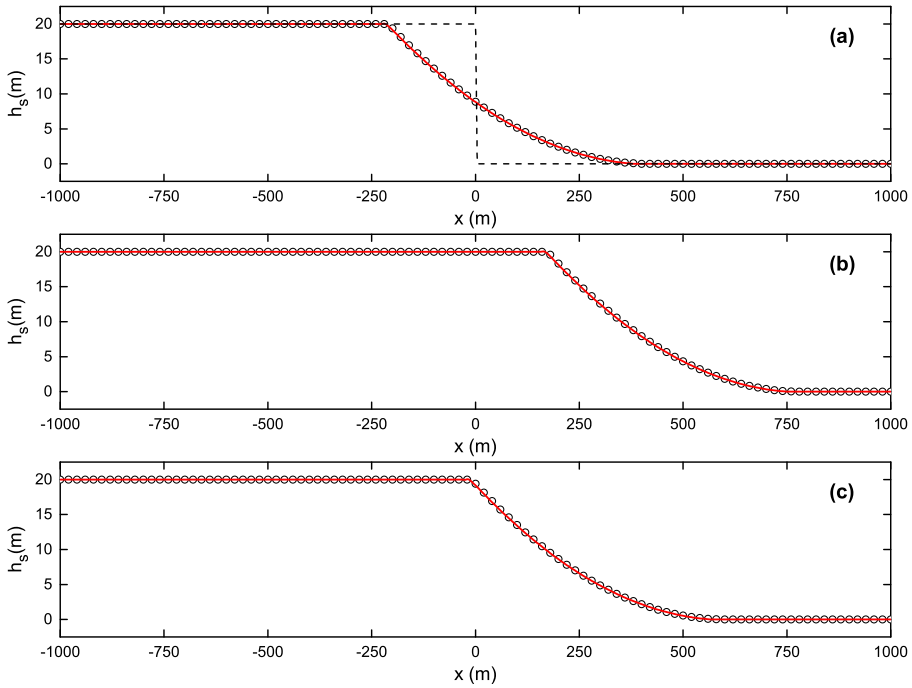


Figure 3: Comparisons of the profile of dam-break flow on a frictional bed between simulated results (solid lines) and analytical solution (circles) at time $t = 15$ s. Top panel (a): bed slope angle $\alpha = 0°$; bed friction angle $\phi_b = 0°$. Middle panel (b): $\alpha = 20°$; $\phi_b = 0°$. Bottom panel (c): $\alpha = 20°$; $\phi_b = 10°$. The initial dam break profile (dashed line) with height $h_0 = 20$ m is also given in panel (a).

Fig. 4 (a) demonstrates granular profile time series from the initiation to the final deposition at $t = 1.6$ s, and Fig. 5 (a) compares the simulated profile of final deposition with the experimental measurements [90] as well as numerical results from Hungr [92] (based on a Lagrangian framework with the SH assumptions) and Yavari-Ramshe [79] (based on the finite volume discretisation with the Q-scheme of Roe). It can be observed that the predicted maximum thickness of the final deposition from the present model agrees well with the measured data, and the front position is also closer to the experimental one than that of Hungr [92]. The time-series distance from the granular front to the initial position shown in Fig. 5 (b) further demonstrates the agreement with experimental data. In general, our simulated results can reasonably represent the final deposition measured in the experiments, although the predicted trailing flow is relatively slow compared to the measurements. This discrepancy was also reported by Yavari-Ramshe [79]. It is thought to be due to the constant friction angle considered in the simulations, while in practice it may vary depending on the flow dynamics; for example, the tail moves in a more fluidized regime while the front flows with more concentrated granular material [49].

We also set-up a numerical test based on the bed that does not include the curvature around the connection between the slope and horizontal domain, i.e. the inclined slope is connected directly with the horizontal domain without the smooth transition. As illustrated in Fig. 4 (b), the resulting granular profiles at $t = 0.6$ s and $t = 1.6$ s are compared with the results considering bed curvature at corresponding times. It is shown that after the granular flow passes the slope transition, that considering the curvature affects the flow velocity significantly. The curved part can in fact accelerate the granular flow, leading to the final position further away from the initial position. In contrast, in the case with a direct connection it seems to play a role more like an obstacle to hinder the flow. This is further illustrated by the computed curved distances shown in Fig. 5 (b).

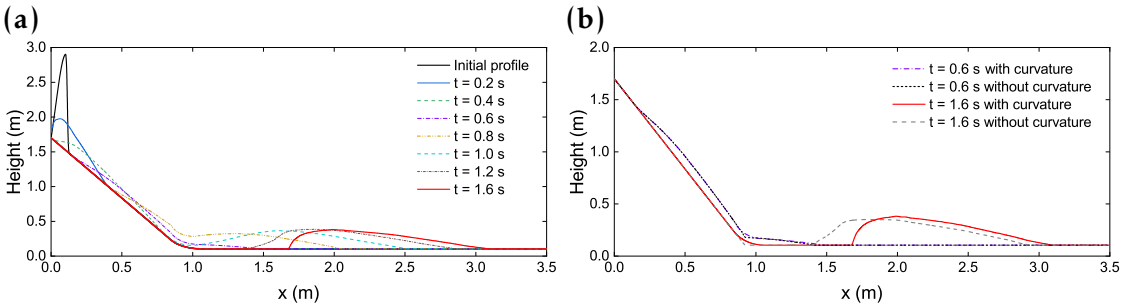


Figure 4: Predicted granular profiles at various time for the bed (a): with the bed curvature and (b): without the bed curvature, i.e. the inclined slope connected directly with the horizontal domain. Their profiles at $t = 0.6$ s and $t = 1.6$ s are also compared in panel (b). For better visualisation the flow thickness in the slope and horizontal domains is exaggerated 2 and 5 times, respectively.

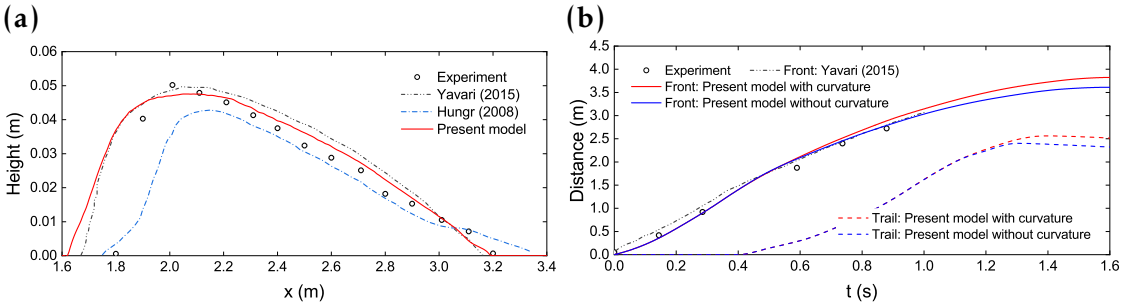


Figure 5: Comparisons of (a) final deposition and (b) time-series curved distance from the granular front to the initial position between the simulated results and measured data [90]. Our numerical results (red solid line) are also compared to the results of Hungr [92] (blue dash-dot) and Yavari-Ramshe [79] (dark grey dash-dot-dot).

4.4. *Impulsive wave generation by a 2D subaerial landslide*

To validate the ability of the coupled two-layer model involving both the granular and wave motions, the results of a laboratory experiment in a 11 m long, 0.5 m wide and 1 m deep wave channel [93] are employed to investigate subaerial landslide impulsive wave generation. [94] presented the laboratory experiment setup in detail. The subaerial landslide made up of granular material initially contained in a box is accelerated under gravity with a pneumatically generated initial velocity.

In the experiments, the still water depth d is 0.3 m, and a series of inner slide box lengths (0.6, 0.3 or 0.15 m) and heights (0.236, 0.118 or 0.059 m) were studied; in the current work only the 0.6 m long and 0.118 m high slide box as shown in Fig. 6 is considered. The landslide made up of the granular material (with a grain diameter $d_g = 4$ mm and a grain density $\rho_s = 2745\,\mathrm{kg/m^3}$) has a bulk density $\rho = 1678\,\mathrm{kg/m^3}$. The internal friction angle is $\phi_i = 34°$ and the dynamic bed friction angle is $\phi_b = 24°$. The initial velocity of the landslide is 3.25 m/s when leaving the slide box. The locations of gauges from the experiment used to record the time evolution of slide profiles and free-surface elevations are also demonstrated in Fig. 6.

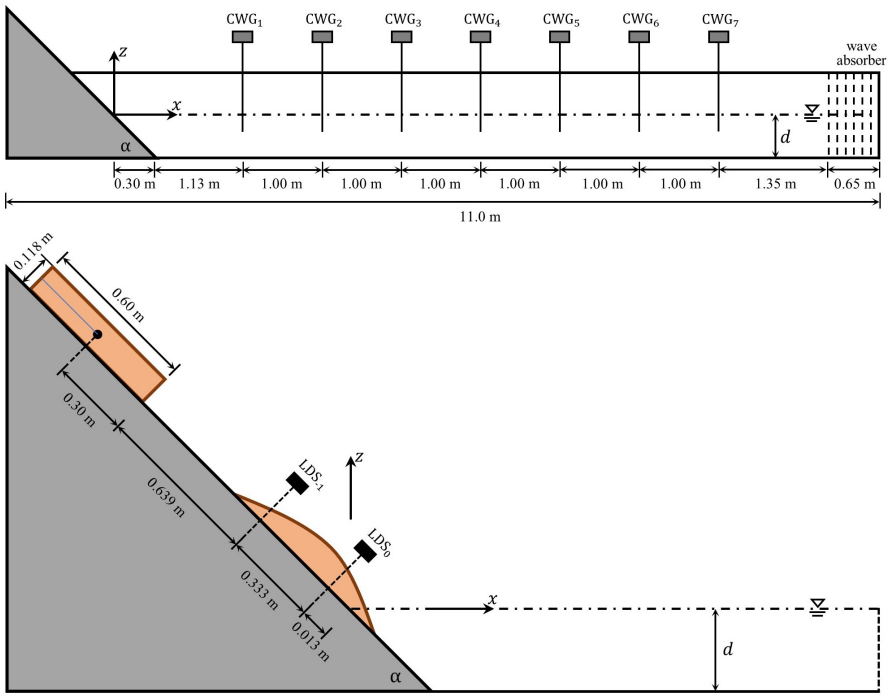


Figure 6: Sketch of the experimental set-up for the [93] laboratory case. The upper panel demonstrates the positions of seven capacitance wave gauges (CWG) recording wave elevations, while the lower panel visualises the positions of the slide and two laser distance sensors (LDS). The slope angle α is 45° and the still water depth d is 0.3 m.

The computational domain has the same length of 11 m as that of the wave channel, which is discretised using a split-quad mesh of 440 triangles ($\Delta x = \Delta y = 0.05$ m). Three layers are used in the vertical in order to allow for the representation of dispersion in the generated impulsive waves. The total time of simulation is 7 s, and the time step size for landslide and wave models is taken as 0.0005 s and 0.005 s, respectively. The earth pressure coefficient $k_{a/p}$ is calculated by (28). As the granular slide is considered to be dry before entering water, we set the parameter $\lambda_1 = \lambda_2 = 0$ and zero fluid pressure in the subaerial environment. After water entry, however, λ_1 and λ_2 in the submarine part of the slide are taken to be 1.0 and 0.5, respectively, and P_h^f is determined through (51).

The wetting and drying depth thresholds for the granular and free-surface flows are 10^{-5} m and 10^{-2} m, respectively.

Since the landslide height and velocity at impact play an important role in accurately simulating the wave generation processes, the simulated slide profiles are first compared with two LDS records in Fig. 7 which also shows numerical profile results from another two-layer model [20] within the numerical framework of NHWAVE [87]. This model uses the same Savage–Hutter theory [48] to treat the slide as a granular flow based on a finite volume method. Below for brevity 'NHWAVE' is used to refer to the two-layer model [20]. Time $t = 0$ s corresponds to the slide's entry into the water. As indicated by Fig. 7, the landslide profile evolution is predicted reasonably well, although the steep tails appearing in the measured profiles are not captured by either our model or NHWAVE. In terms of the slide height good agreement is found, particularly as compared to the over-estimation given by NHWAVE. In addition, the landslide frontal speed can be calculated based on the time lag between the two profiles; the well-predicted slide front location implies that the speed of the slide front is also represented accurately.

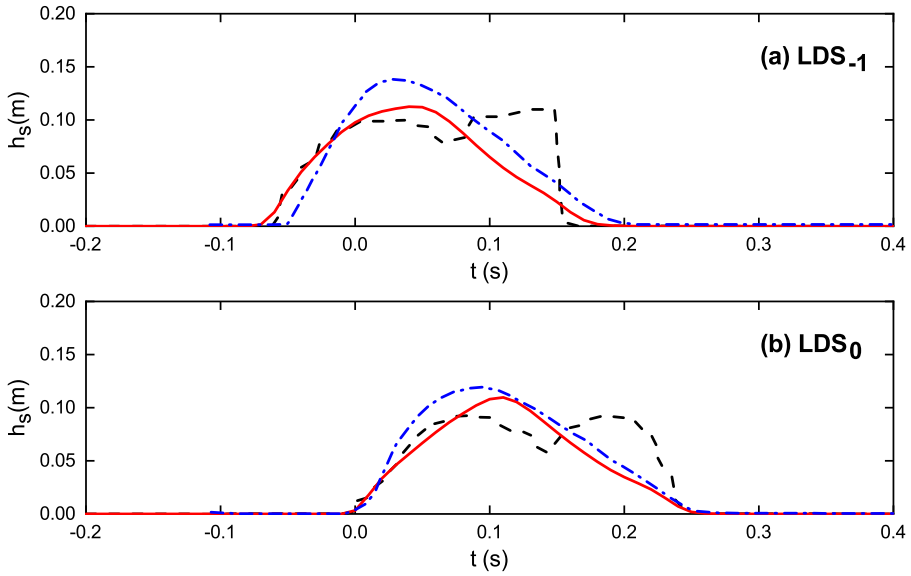


Figure 7: Landslide profile time series at upper panel (a) LDS_{-1} and lower panel (b) LDS_0. Measurements (black dashed lines) are used to compare against simulated results from our granular model (red solid) and from NHWAVE (blue dash-dot) [20] using the same theoretical framework of granular flow [48].

Fig. 8 compares the simulated landslide-generated wave elevations with the recorded data at gauge 2–7. The observed good agreement indicates that the presented model implements the mechanism of wave generation reasonably and represents the subsequent impulsive wave motions correctly. Compared against the over-estimation of the leading wave amplitude and the significant water level drawdown in the numerical results of NHWAVE [20], our model captures the main peaks and overall phase structure with less discrepancy. It may also be noted that after the normalised time $t\sqrt{g/d} > 30$ the surface elevations at gauges 5–7 are affected by reflected waves. Although a numerical sponge layer is used near the right-hand side boundary to diminish the reflection, due to the close distance between the gauges and the boundary the reflected waves are not totally absorbed. In addition, the simulated results from the present model with only considering the hydrostatic pressure (depending only on the water height) at the landslide-water interface are also given in Fig. 8. The comparisons demonstrate that the non-hydrostatic pressure imposed at the landslide-water interface can play an important role in the slide motion and its shape evolution, and thus the resulting slide deformation in turn affects

the free-surface wave fluctuation. In this case, the upper-layer water pressure seems to push back against the granular landslide to prevent its sliding movement.

Fig. 9 displays raw PIV images recorded in the experiment [94] showing the simultaneous granular landslide and generated wave dynamics, which are also compared against the simulation results. As shown by panels (b)–(e) in the figure, after reaching the horizontal flat domain, the simulated slide motion is faster than that in the experiment, and the resulting predicted location is significantly overestimated by the present model. One of the possible reasons could be that the basal friction angle in practice may increase after the slide passes the slope transition to the horizontal domain, while in this study we only consider constant values for both the internal and basal friction angles. Moreover, the complicated landslide-water interaction is simplified in our model such that the landslide and water remain in contact without the entrainment of large air cavities. For this case with such a large initial velocity (3.25 m/s) compared to its length scale, the impact effects should be important and the resulting resistance cannot be ignored. However, the present model does not account for this possible velocity reduction from the significant landslide-water interaction during water entry. With the gravitational driving force vanishing, the slide will come to rest on the plane bed due to the basal friction. In the simulation, the landslide is almost at rest at the normalised time $t\sqrt{g/d} = 5.72$, and its predicted slide height of final deposition is very close to that in the experiment, although the centroid location (around $x/d = 4.7$) is obviously over-estimated. A similar overestimation of the final position was also reported by [20], and it should be noticed that the predicted slide length (around 3.7 m) at the deposition by the present model is very close to that by NHWAVE [20]. Fig. 9 also shows the time-series slide profiles and water levels from the simulation with only hydrostatic pressure of the water waves considered, and the discrepancy further indicates the importance of the non-hydrostatic pressure effects for an accurate assessment of impulsive wave generation by deformable landslides in certain parameter regimes.

4.5. Impulsive wave generation by a 3D subaerial landslide

In this section, impulsive wave generation by a 3D granular landslide is further studied based on the laboratory experiments of [38] in a wave basin of 48.8 m in length and 26.5 m in width. Varying still water depths of $d = 0.3$, 0.6, 0.9 and 1.2 m are considered in the experiments; in the case chosen for comparison here, however, only a still water depth of 0.6 m is adopted. The subaerial landslide is initially contained in a slide box (1.05 m long, 1.2 m wide and 0.3 m high) and is accelerated on a slope with an incline of 27.1°, as demonstrated in Fig. 10. The slide comprises of river gravel with sizes 6.35 mm ~ 19.05 mm, a grain density $\rho_g = 2600\,\mathrm{kg/m^3}$, a landslide bulk density $\rho = 1760\,\mathrm{kg/m^3}$, an internal friction angle $\phi_i = 41°$ and bed friction angle $\phi_b = 23°$ [20, 95].

Due to symmetry about the $y = 0$ plane in this case, the computational domain only includes half of the physical domain in y. The 13.25 m wide half-domain has been extended to 17 m with a sponge layer to diminish reflected waves; it is discretised using 240 and 85 elements in the $x-$ and $y-$ directions, respectively, yielding the resulting mesh with an edge length of 0.2 m. To simulate the dispersive wave flow, three layers in the vertical are used. The entire simulation period is 20 s, and the time step size for granular and wave models is 0.05 s and 0.005 s, respectively. During the simulation, wetting and drying processes occur around the shoreline. The wetting and drying parameters for the granular and wave motions are $\epsilon = 10^{-4}$ and $\delta = 5\times10^{-2}$ m, respectively. The subaerial landslide is initially located in the middle of the slope, and the simulation adopts the same granular parameters as those in the experiment, except that the range of grain sizes is approximated with the inter-granular stresses using a Coulomb friction approach. Before the slide enters water, the parameter λ_1 and λ_2 are both expected as zero, whereas for the submarine part of the slide λ_1 an λ_2 are adjusted to 1.0 and 0.5,

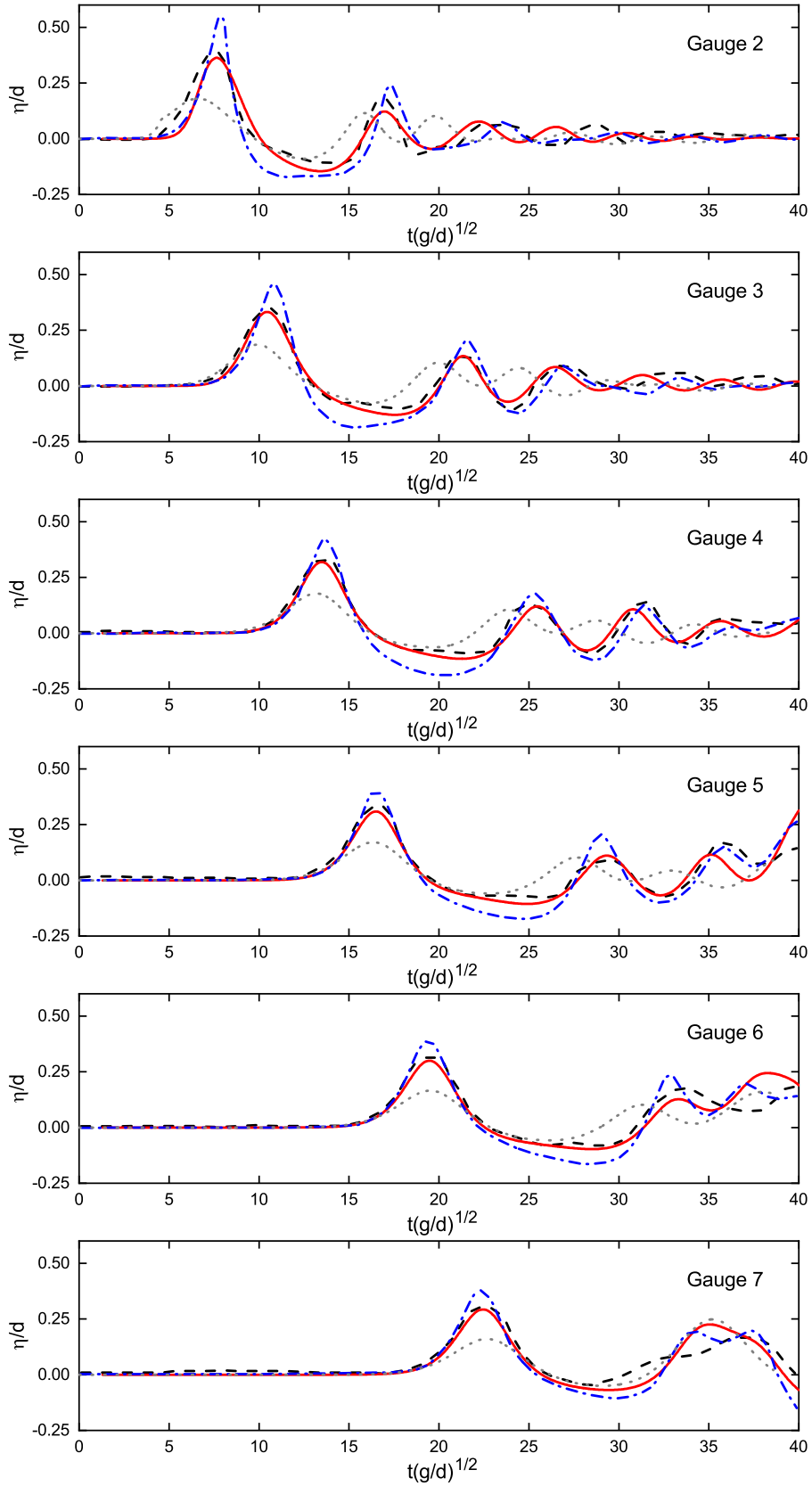


Figure 8: Free-surface elevation time series at gauges 2–7 for the impulsive wave generation by a 2D sub-aerial landslide [93]. Simulated results from the present model (red solid lines) are compared with both the recorded data (black dashed) and NHWAVE's results (blue dash-dot) [20]. The numerical results from the present model without considering the non-hydrostatic pressure at the landslide-water interface are shown by the grey dotted lines.

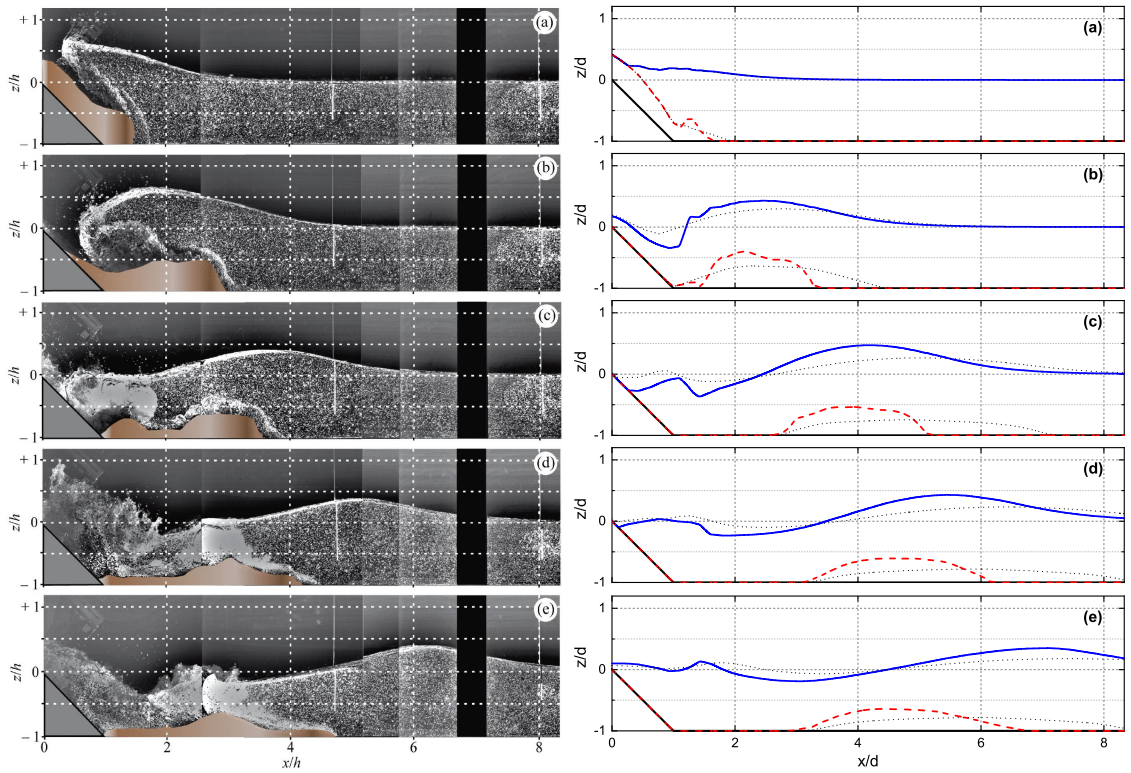


Figure 9: Comparisons between measured [from 94] (left) and simulated (right) slide profiles and water levels at normalised times $t\sqrt{g/d}$ = (a) 1.14, (b) 2.29, (c) 3.43, (d) 4.57 and (e) 5.72. The time $t\sqrt{g/d} = 0$ corresponds to the slide impacting the water. The simulated slide profiles and water levels are represented by the red dashed and blue solid lines, respectively. The black solid lines show the bottom geometry, and the grey dotted lines represents the results from the simulation that does not account for the non-hydrostatic pressure at the slide interface.

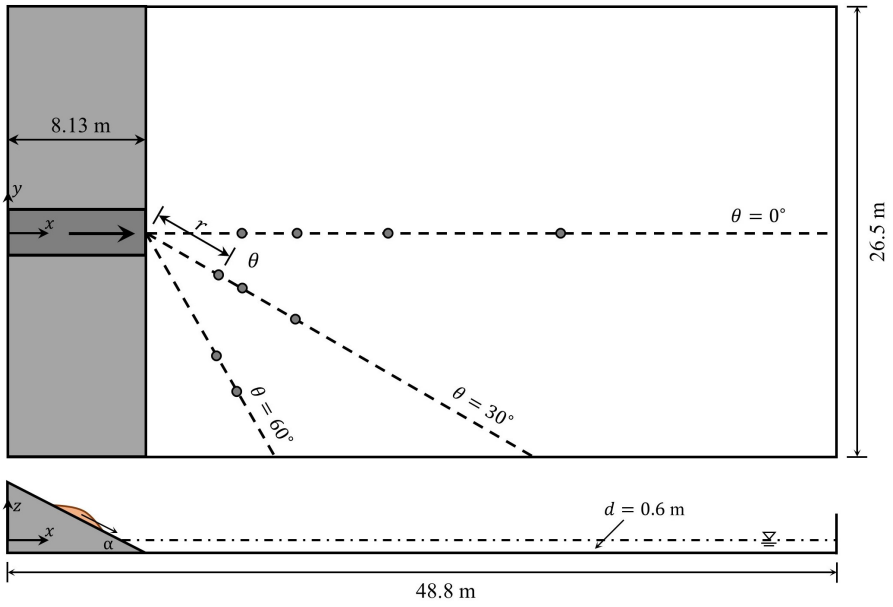


Figure 10: Sketch of the experimental set-up for the [38] case. The grey dots show the positions of the wave gauge array: (a) $\theta = 0°$, r/d = 9.0, 14.2, 23.3, 40.2, (b) $\theta = 30°$, r/d = 7.7, 10.3, 16.4 and (c) $\theta = 60°$, r/d = 13.3, 17.3, where θ refers to the angular direction and r denotes the radial propagation distance. The still water depth d considered here is 0.6 m and the slope angle α is 27.1°.

respectively, based on where the unmodified water depth is positive (the wet part of the domain).

Fig. 11 compares the simulated surface elevations (for our model as well as that of [20]) with experimental measurements at nine wave gauges. In general, good agreement can be observed especially in terms of the leading waves, indicating that the dynamics of the impulsive waves are represented reasonably well by the proposed model. Compared to measured data, the numerical results of NHWAVE [20] demonstrate significant over-estimation of leading wave elevations, which further indicates that our model is capturing the overall wave structure reasonably well.

Fig. 12 displays the numerical results based on the wave model using the hydrostatic assumption, i.e. not solving the Poisson equation for the non-hydrostatic pressure, and compares them with the non-hydrostatic ones. Compared to the non-hydrostatic results that consist of a series of waves due to dispersion, the hydrostatic ones do not represent wave dispersion correctly and the larger wave with steep wave front indicates that the wave energy is concentrated mostly in this leading wave. This is further shown by the snapshots of the wave patterns in Fig. 14, where the left panel corresponding to the hydrostatic simulation illustrates the absence of a generated wave train. These results demonstrate that non-hydrostatic pressure can play a key role in the accurate representation of landslide-induced dispersive waves.

Fig. 12 also evaluates the sensitivity of the simulated wave elevations to the parameter λ_2, with results obtained using $\lambda_2 = 0.2$ and $\lambda_2 = 0.5$ compared. The parameter λ_2 controls what percent of the normal pressure comes from the fluid phase through the lower layer, and hence determines the pore pressure at the bed. Specifically, $\lambda_2 = 0$ represents constant fluid pressure inside the landslide layer from the landslide-water interface to the bed. It is noted that the parameter λ used in NHWAVE [20] is similar to the combination of parameters r and λ_2 considered in the present model, where $r = \frac{\rho^f}{\rho}$ represents the ratio between the water density and the mixture density and $r\lambda_2$ can together influence the magnitude of Coulomb friction. Fig. 12 shows that based on the same value of r a smaller value of λ_2, i.e. larger Coulomb friction retarding the granular slide motion, leads to decreased peak wave heights and slower wave propagation. Compared to the leading wave, the wave train appearing after the leading wave is more affected by the value of λ_2, since before water entry the slide is considered as fully dry (i.e. $\lambda_2 = 0$) and hence the variation of this parameter starts to make a difference after water entry and has a larger influences on the subsequent wave generation. Furthermore, the parameter λ_2 more strongly affects the impulsive waves near the wave generating zone, as demonstrated by the decreasing discrepancy of wave elevations from panel (a) to panel (d) in Fig. 12. Similar results were given by [20].

The simulated landslide motion is demonstrated by the snapshots in Fig 13. Compared to the 2D vertical-slice subaerial-landslide case illustrated above, the 3D slide motion with lateral spreading is more complex. During the slide motion, its width grows significantly owing to the retarding effects of the dry slope bed and the water after impact. It is clear to observe that the slide starts to pile up after reaching the plane bed (e.g. compare frames at $t = 3$s and $t = 4$s). Although the slide deposits around the slope transition, the radial waves as seen in the right panel of Fig. 14 develop due to the initial wave crests generated by the slide impact and the subsequent water displacement from the wave run-up and run-down along the adjacent slope. The simulated final deposition of the granular material is compared with measurement in Fig. 15. Consistent with what can be observed in Fig. 13, the final deposition is found around the bed slope transition. Compared to the measured deposition, the simulated one is located further offshore, and has a much reduced slide height. The significant discrepancy is expected due to the fact that in the experiments the lateral spread is confined before water entry (see their figure

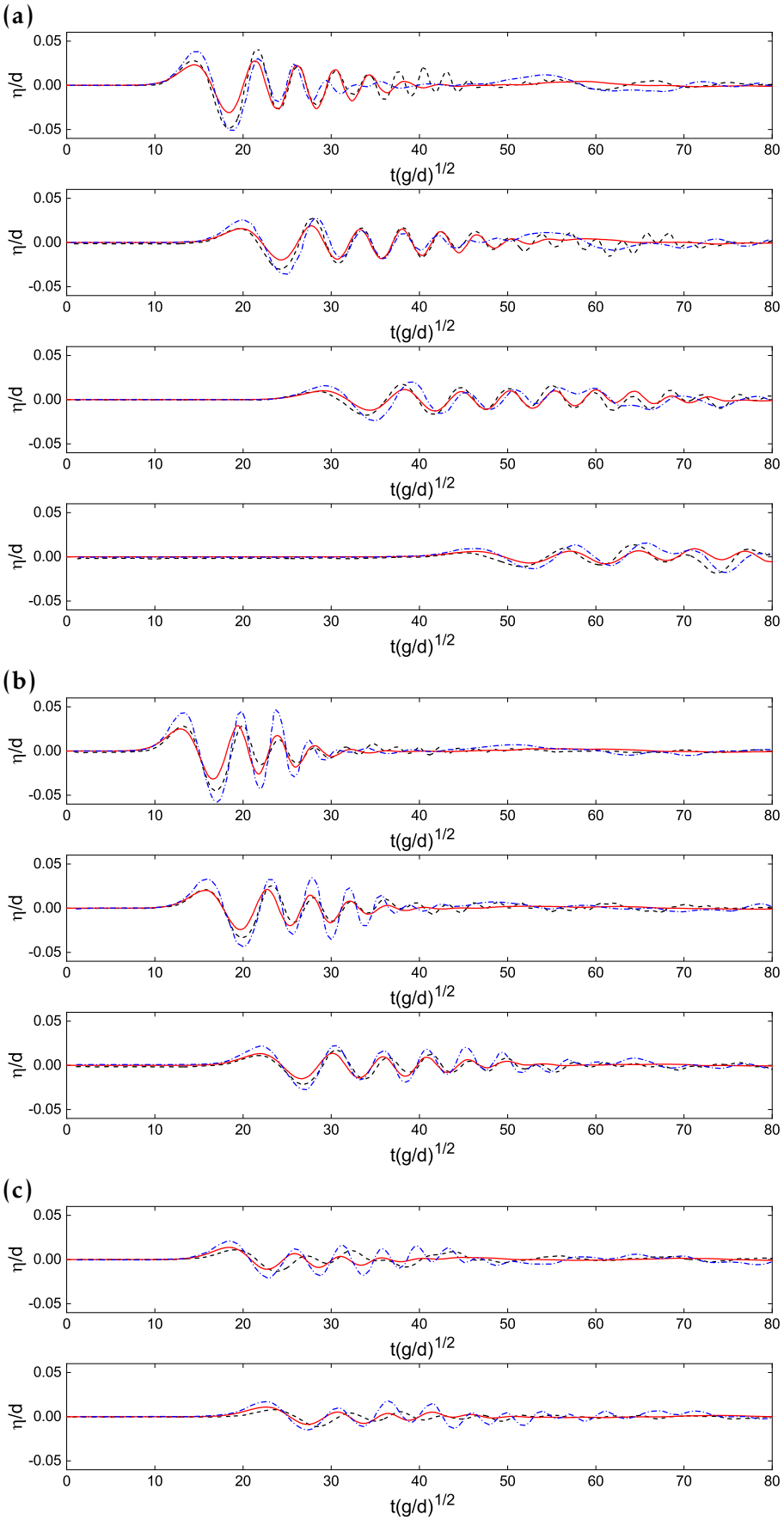


Figure 11: Time-series of free-surface elevations at (a) $\theta = 0°$, $r/d = 9.0$, 14.2, 23.3, 40.2, (b) $\theta = 30°$, $r/d = 7.7$, 10.3, 16.4 and (c) $\theta = 60°$, $r/d = 13.3$, 17.3, for impulsive wave generation by a 3D subaerial landslide [38]. Laboratory measurements (black dashed lines) are compared with simulated results from the present model (red solid) and from NHWAVE (blue dash-dot) [20].

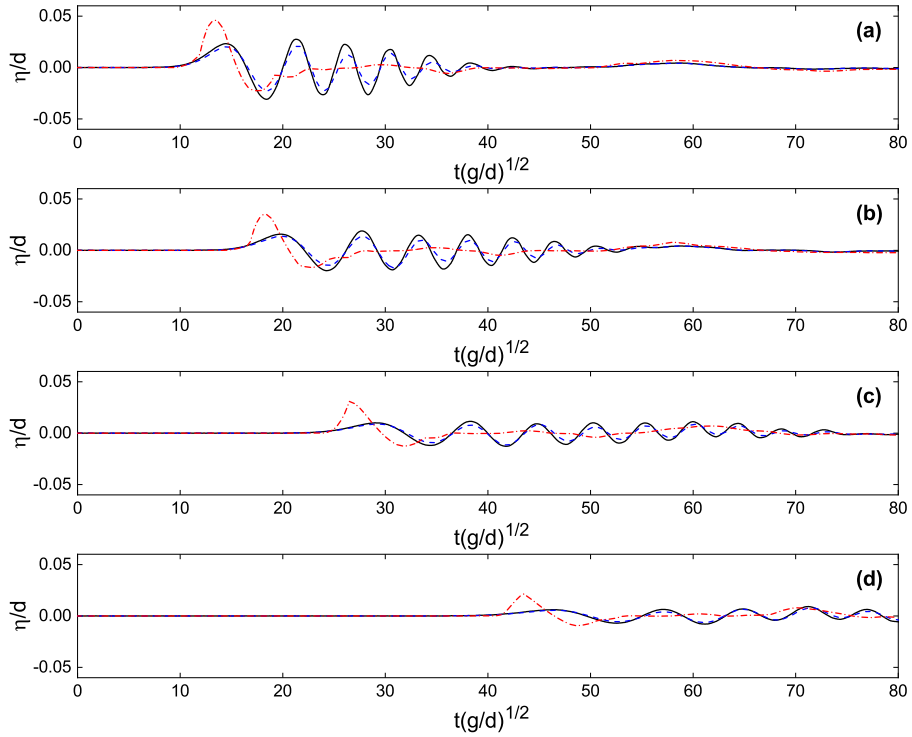


Figure 12: Free-surface elevation time series at $\theta = 0°$, r/d = (a) 9.0, (b) 14.2, (c) 23.3 and (d) 40.2 for the 3D subaerial landslide generated waves. The hydrostatic numerical results (red dash-dot lines) are compared with non-hydrostatic results with $\lambda_2 = 0.5$ (black solid) and $\lambda_2 = 0.2$ (blue dash).

3 and 4 in [38]), but in the present numerical simulation the slide moves freely after initiation and has spread more laterally. Assuming volume conservation, it can to a certain degree be explained why there is such a big difference between the high level of the experimental slide and the low level of predicted slide along the symmetry axis ($y = 0$). In terms of the discrepancy of final deposition with the lab results, a further possible explanation is the constant representation of Coulomb friction angles at the slope transition and the simplification of the landslide-water interaction. It is noted that compared with the results of NHWAVE [20], the present model produces similar results.

5. Conclusions

In this paper a new two-layer granular landslide wave generation model is developed based on a discontinuous Galerkin finite element discretisation. The lower layer describes landslide deformation which is treated as a granular debris flow and is solved using a depth-averaged granular model with inter-granular stresses considered. Coupled with this granular lower layer, the upper layer is formulated as a vertically resolved free-surface flow using a previously developed non-hydrostatic coastal ocean model with a σ-coordinate transformation used in the vertical [47].

Compared to the prior models of [21, 87], which are based on a flat local coordinate system, the present granular flow model introduces bed curvature to enable a varying bed slope angle. The resulting model equations are first derived in a local coordinate system and then transferred to a global Cartesian coordinate system. In this way both the granular landslide and impulsive waves are represented in the Cartesian coordinate system, and hence the exchange of variable values in the coupling between the landslide and wave flow equations are more straightforward compared to if they are formulated in different coordinate systems.

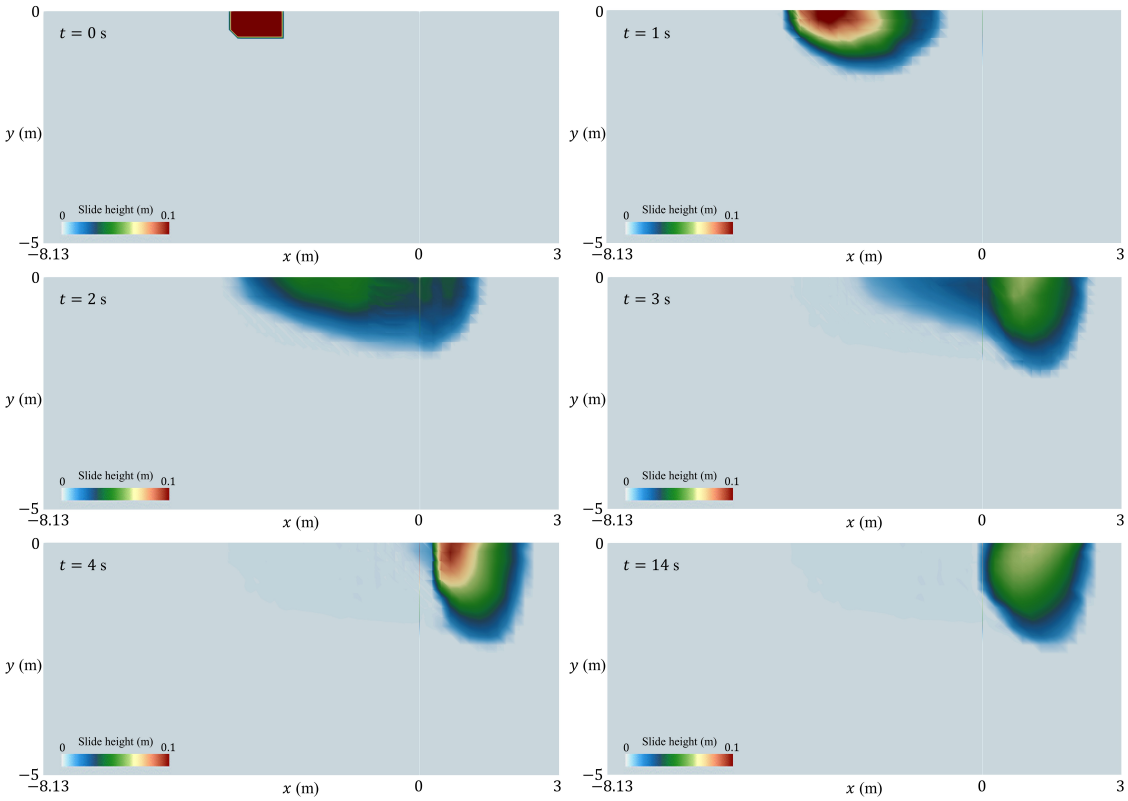


Figure 13: Granular landslide motions in a plan view ((x, y)-coordinate) along the slope at $t = 0$ (initial), 1, 2, 3, 4 and 14 s (almost completely deposited). The white lines at $x = 0$ indicate the slope transition. The colour scale for the landslide thickness ranges between 0 to 0.1 m based on a blue-green-orange colour variation for all frames.

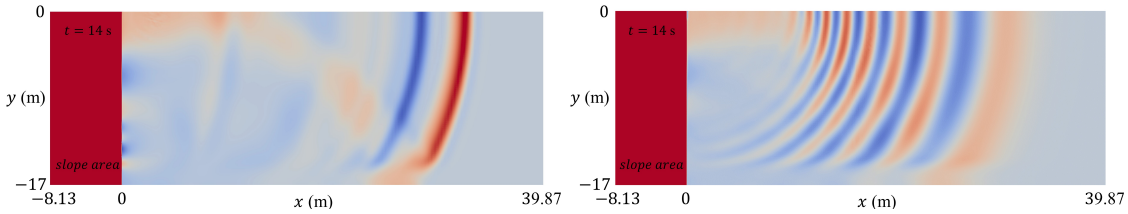


Figure 14: Wave patterns in a plan view ((x, y)-coordinate) at t = 14 s generated by a 3D subaerial landslide. Left and right panels denote results from the hydrostatic and non-hydrostatic simulations, respectively. The colour scale for the surface wave elevation ranges between -0.006 m to 0.008 m based on a blue-red colour variation.

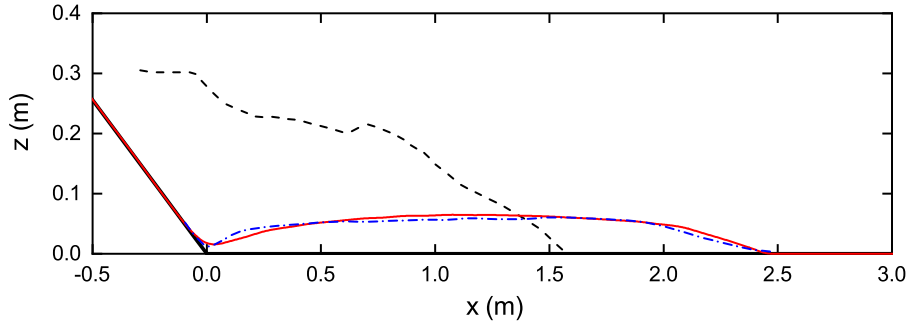


Figure 15: Final deposition along the symmetry axis ($y = 0$) for the 3D granular landslide. Our numerical results (red solid line) are compared to NHWAVE's results (blue dash-dot) [20] as well as measured data (black dash) [38].

The presented two-layer model uses a coupled time integration scheme and a novel wetting and drying scheme to avoid an artificial pressure gradient. A series of test cases have been used to validate the model. The first stationary case was used to ensure that the model is capable of preserving the stationary solution, followed by two cases only involving granular flows to validate the model's accuracy in treating the wetting and drying discontinuity through the implementation of a HLLC Riemann solver. Subsequent validation against laboratory experiments demonstrated that the model can efficiently represent landslide-water interaction. Although the developed model and its numerical techniques were demonstrated to successfully predict granular landslide motion from initiation to deposition as well as impulsive wave generation by 2D and 3D landslides, limitations of the current study and model should also be acknowledged.

In addition to the long wave approximation, the fluid normal stress in the granular layer is assumed to be linearly dependent on the landslide depth, and the fluid shear stresses at the landslide-water interface are neglected. The interaction between the lower landslide and upper water layer is simplified by assuming that they remain in contact, and hence complicated processes such as the entrainment of large air cavities cannot be represented. In addition, the local slope angle introduced in the present work to take the effects of bottom curvature into account assumes small variations in curvature, and for relatively large slope curvatures the current model may not be as accurate. Thus, the assumptions and simplifications exploited in deriving the mathematical formulation may limit the applicability of the present model and affect the accuracy in studying some cases with significant landslide-water interaction. Furthermore, the current study only introduces along-slope bed curvature and arbitrary bed curvature is not considered, which further limits the model's application to realistic cases. In future work further extension of the present model could focus on permitting landslide motion over more irregular bathymetry, i.e. accounting for lateral variations. Other potential areas for future study include comparing wave generation by landslides with various rheologies, as well as benchmarking against real subaerial and submarine landslide cases

Acknowledgements

This study is jointly supported by National Natural Science Foundation of China under grant No. 41961144014, and the UK's Engineering and Physical Sciences Research Council (EPSRC) under grants EP/M011054/1, EP/L000407/1 and EP/R029423/1.

Computer code availability

This work is based upon the coastal ocean model *Thetis*, of which the code base can be found at https://github.com/thetisproject/thetis. For the two-layer model presented in this work, the full code can be accessed through https://github.com/wei-pan/thetis-nh.

References

[1] S. Yavari-Ramshe, B. Ataie-Ashtiani, Numerical modeling of subaerial and submarine landslide-generated tsunami waves—recent advances and future challenges, Landslides 13 (6) (2016) 1325–1368.

[2] B. W. Levin, M. Nosov, et al., Physics of tsunamis, Vol. 327, Springer, 2009.

[3] H. Yeh, V. Titov, V. Gusiakov, E. Pelinovsky, V. Khramushin, V. Kaistrenko, The 1994 Shikotan earthquake tsunamis, Pure and Applied Geophysics 144 (3-4) (1995) 855–874.

[4] I. V. Fine, A. B. Rabinovich, B. Bornhold, R. Thomson, E. A. Kulikov, The grand banks landslide-generated tsunami of november 18, 1929: preliminary analysis and numerical modeling, Marine Geology 215 (1-2) (2005) 45–57.

[5] H. M. Fritz, Lituya bay case rockslide impact and wave run-up, Science of tsunami Hazards 19 (1) (2001) 3–22.

[6] U. Ten Brink, J. Chaytor, E. L. Geist, D. S. Brothers, B. D. Andrews, Assessment of tsunami hazard to the us atlantic margin, Marine Geology 353 (2014) 31–54.

[7] D. R. Tappin, The generation of tsunamis, Encyclopedia of maritime and offshore engineering (2017) 1–10.

[8] W.-F. Peng, C.-L. Wang, S.-T. Chen, S.-T. Lee, Incorporating the effects of topographic amplification and sliding areas in the modeling of earthquake-induced landslide hazards, using the cumulative displacement method, Computers & geosciences 35 (5) (2009) 946–966.

[9] S. N. Ward, Landslide tsunami, Journal of Geophysical Research: Solid Earth 106 (B6) (2001) 11201–11215.

[10] N. Mori, T. Takahashi, T. Yasuda, H. Yanagisawa, Survey of 2011 tohoku earthquake tsunami inundation and run-up, Geophysical research letters 38 (7) (2011).

[11] B. A. Bolt, W. Horn, G. A. MacDonald, R. Scott, Geological Hazards: Earthquakes-tsunamis-volcanoes-avalanches-landslides-floods, Springer Science & Business Media, 2013.

[12] L. Jiang, P. H. LeBlond, The coupling of a submarine slide and the surface waves which it generates, Journal of Geophysical Research: Oceans 97 (C8) (1992) 12731–12744.

[13] S. Assier-Rzadkieaicz, P. Heinrich, P. Sabatier, B. Savoye, J. Bourillet, Numerical modelling of a landslide-generated tsunami: the 1979 nice event, Pure and Applied Geophysics 157 (10) (2000) 1707–1727.

[14] L. Lobkovsky, R. Mazova, I. Remizov, N. Baranova, Local tsunami run-up depending on initial localization of the landslide body at submarine slope, Landslides (2020) 1–11.

[15] P. Lynett, P. L.-F. Liu, A numerical study of submarine–landslide–generated waves and run–up, Proceedings of the Royal Society of London. Series A: Mathematical, Physical and Engineering Sciences 458 (2028) (2002) 2885–2910.

[16] D. R. Fuhrman, P. A. Madsen, Tsunami generation, propagation, and run-up with a high-order boussinesq model, Coastal Engineering 56 (7) (2009) 747–758.

[17] H. Zhou, C. Moore, Y. Wei, V. Titov, A nested-grid boussinesq-type approach to modelling dispersive propagation and runup of landslide-generated tsunamis, Natural Hazards and Earth System Sciences 11 (10) (2011) 2677–2697.

[18] D. Dutykh, H. Kalisch, Boussinesq modeling of surface waves due to underwater landslides, Nonlinear Processes in Geophysics 20 (3) (2013) 267–285.

[19] G. Ma, J. T. Kirby, F. Shi, Numerical simulation of tsunami waves generated by deformable submarine landslides, Ocean Modelling 69 (2013) 146–165.

[20] G. Ma, J. T. Kirby, T.-J. Hsu, F. Shi, A two-layer granular landslide model for tsunami wave generation: Theory and computation, Ocean Modelling 93 (2015) 40–55.

[21] P. Si, J. Aaron, S. McDougall, J. Lu, X. Yu, N. J. Roberts, J. J. Clague, A non-hydrostatic model for the numerical study of landslide-generated waves, Landslides 15 (4) (2018) 711–726.

[22] W. Pan, S. C. Kramer, T. Kärnä, M. D. Piggott, Comparing non-hydrostatic extensions to a discontinuous finite element coastal ocean model, Ocean Modelling (2020) 101634.

[23] P. Watts, S. T. Grilli, et al., Underwater landslide shape, motion, deformation, and tsunami generation, in: The Thirteenth International Offshore and Polar Engineering Conference, International Society of Offshore and Polar Engineers, 2003.

[24] P.-F. Liu, T.-R. Wu, F. Raichlen, C. Synolakis, J. Borrero, Runup and rundown generated by three-dimensional sliding masses, Journal of fluid Mechanics 536 (2005) 107–144.

[25] D. Yuk, S. Yim, P.-F. Liu, Numerical modeling of submarine mass-movement generated waves using rans model, Computers & geosciences 32 (7) (2006) 927–935.

[26] S. Abadie, J. Harris, S. Grilli, R. Fabre, Numerical modeling of tsunami waves generated by the flank collapse of the cumbre vieja volcano (la palma, canary islands): Tsunami source and near field effects, Journal of Geophysical Research: Oceans 117 (C5) (2012).

[27] J. Horrillo, A. Wood, G.-B. Kim, A. Parambath, A simplified 3-d navier-stokes numerical model for landslide-tsunami: Application to the gulf of mexico, Journal of Geophysical Research: Oceans 118 (12) (2013) 6934–6950.

[28] P. Si, H. Shi, X. Yu, Development of a mathematical model for submarine granular flows, Physics of Fluids 30 (8) (2018) 083302.

[29] P. Si, H. Shi, X. Yu, A general numerical model for surface waves generated by granular material intruding into a water body, Coastal Engineering 142 (2018) 42–51.

[30] S. T. Grilli, S. Vogelmann, P. Watts, Development of a 3d numerical wave tank for modeling tsunami generation by underwater landslides, Engineering analysis with boundary elements 26 (4) (2002) 301–313.

[31] A. Serrano-Pacheco, J. Murillo, P. García-Navarro, A finite volume method for the simulation of the waves generated by landslides, Journal of hydrology 373 (3-4) (2009) 273–289.

[32] C. Cecioni, G. Bellotti, Modeling tsunamis generated by submerged landslides using depth integrated equations, Applied Ocean Research 32 (3) (2010) 343–350.

[33] J. Hill, G. S. Collins, A. Avdis, S. C. Kramer, M. D. Piggott, How does multiscale modelling and inclusion of realistic palaeobathymetry affect numerical simulation of the storegga slide tsunami?, Ocean Modelling 83 (2014) 11–25.

[34] R. C. Smith, J. Hill, S. L. Mouradian, M. D. Piggott, G. S. Collins, A new methodology for performing large scale simulations of tsunami generated by deformable submarine slides, Ocean Modelling (2021).

[35] J. Imran, P. Harff, G. Parker, A numerical model of submarine debris flow with graphical user interface, Computers & geosciences 27 (6) (2001) 717–729.

[36] B. Ataie-Ashtiani, A. Nik-Khah, Impulsive waves caused by subaerial landslides, Environmental Fluid Mechanics 8 (3) (2008) 263–280.

[37] H. M. Fritz, W. H. Hager, H.-E. Minor, Landslide generated impulse waves., Experiments in Fluids 35 (6) (2003) 505–519.

[38] F. Mohammed, H. M. Fritz, Physical modeling of tsunamis generated by three-dimensional deformable granular landslides, Journal of Geophysical Research: Oceans 117 (C11) (2012).

[39] V. Heller, J. Spinneken, Improved landslide-tsunami prediction: effects of block model parameters and slide model, Journal of Geophysical Research: Oceans 118 (3) (2013) 1489–1507.

[40] P. Watts, Water waves generated by underwater landslides, Ph.D. thesis, California Institute of Technology (1997).

[41] I. V. Fine, A. B. Rabinovich, R. E. Thomson, E. A. Kulikov, Numerical modeling of tsunami generation by submarine and subaerial landslides, in: Submarine landslides and tsunamis, Springer, 2003, pp. 69–88.

[42] B. Ataie-Ashtiani, A. Najafi-Jilani, Laboratory investigations on impulsive waves caused by underwater landslide, Coastal Engineering 55 (12) (2008) 989–1004.

[43] A. Skvortsov, B. Bornhold, Numerical simulation of the landslide-generated tsunami in kitimat arm, british columbia, canada, 27 april 1975, Journal of Geophysical Research: Earth Surface 112 (F2) (2007).

[44] S. A. Rzadkiewicz, C. Mariotti, P. Heinrich, Numerical simulation of submarine landslides and their hydraulic effects, Journal of Waterway, Port, Coastal, and Ocean Engineering 123 (4) (1997) 149–157.

[45] P. Gauer, A. Elverhoi, D. Issler, F. V. De Blasio, On numerical simulations of subaqueous slides: back-calculations of laboratory experiments of clay-rich slides, Norsk Geologisk Tidsskrift 86 (3) (2006) 295.

[46] R. C. Smith, J. Hill, G. S. Collins, M. D. Piggott, S. C. Kramer, S. D. Parkinson, C. Wilson, Comparing approaches for numerical modelling of tsunami generation by deformable submarine slides, Ocean Modelling 100 (2016) 125–140.

[47] W. Pan, S. C. Kramer, M. D. Piggott, A σ-coordinate non-hydrostatic discontinuous finite element coastal ocean model, Ocean Modelling 157 (2021) 101732.

[48] S. B. Savage, K. Hutter, The motion of a finite mass of granular material down a rough incline, Journal of fluid mechanics 199 (1989) 177–215.

[49] R. M. Iverson, The physics of debris flows, Reviews of geophysics 35 (3) (1997) 245–296.

[50] R. M. Iverson, D. L. George, A depth-averaged debris-flow model that includes the effects of evolving dilatancy. i. physical basis, Proceedings of the Royal Society A: Mathematical, Physical and Engineering Sciences 470 (2170) (2014) 20130819.

[51] P. Heinrich, A. Piatanesi, H. Hebert, Numerical modelling of tsunami generation and propagation from submarine slumps: the 1998 papua new guinea event, Geophysical Journal International 145 (1) (2001) 97–111.

[52] E. D. Fernández-Nieto, F. Bouchut, D. Bresch, M. C. Diaz, A. Mangeney, A new savage–hutter type model for submarine avalanches and generated tsunami, Journal of Computational Physics 227 (16) (2008) 7720–7754.

[53] J. Macías, J. Vázquez, L. Fernández-Salas, J. González-Vida, P. Bárcenas, M. Castro, V. Díaz-del Río, B. Alonso, The al-borani submarine landslide and associated tsunami. a modelling approach, Marine Geology 361 (2015) 79–95.

[54] S. Yavari-Ramshe, B. Ataie-Ashtiani, A rigorous finite volume model to simulate subaerial and submarine landslide-generated waves, Landslides 14 (1) (2017) 203–221.

[55] P. Heinrich, A. Mangeney, S. Guibourg, R. Roche, G. Boudon, J.-L. Cheminée, Simulation of water waves generated by a potential debris avalanche in montserrat, lesser antilles, Geophysical Research Letters 25 (19) (1998) 3697–3700.

[56] T. Giachetti, R. Paris, K. Kelfoun, F. J. Pérez-Torrado, Numerical modelling of the tsunami triggered by the güimar debris avalanche, tenerife (canary islands): comparison with field-based data, Marine Geology 284 (1-4) (2011) 189–202.

[57] A. Lacasta, C. Juez, J. Murillo, P. García-Navarro, An efficient solution for hazardous geophysical flows simulation using gpus, Computers & Geosciences 78 (2015) 63–72.

[58] W. Liu, S. He, A two-layer model for simulating landslide dam over mobile river beds, Landslides 13 (3) (2016) 565–576.

[59] C. Zhang, J. T. Kirby, F. Shi, G. Ma, S. T. Grilli, A two-layer non-hydrostatic landslide model for tsunami generation on irregular bathymetry. 1. theoretical basis, Ocean Modelling 159 (2021) 101749.

[60] F. Bouchut, A. Mangeney-Castelnau, B. Perthame, J.-P. Vilotte, A new model of saint venant and savage–hutter type for gravity driven shallow water flows, Comptes rendus mathematique 336 (6) (2003) 531–536.

[61] T. Capone, A. Panizzo, J. J. Monaghan, Sph modelling of water waves generated by submarine landslides, Journal of Hydraulic Research 48 (sup1) (2010) 80–84.

[62] V. Heller, M. Bruggemann, J. Spinneken, B. D. Rogers, Composite modelling of subaerial landslide–tsunamis in different water body geometries and novel insight into slide and wave kinematics, Coastal Engineering 109 (2016) 20–41.

[63] A. Xenakis, S. Lind, P. Stansby, B. D. Rogers, Landslides and tsunamis predicted by incompressible smoothed particle hydrodynamics (sph) with application to the 1958 lituya bay event and idealized experiment, Proceedings of the Royal Society A: Mathematical, Physical and Engineering Sciences 473 (2199) (2017) 20160674.

[64] W.-J. Xu, Z.-G. Yao, Y.-T. Luo, X.-Y. Dong, Study on landslide-induced wave disasters using a 3d coupled sph-dem method, Bulletin of Engineering Geology and the Environment 79 (1) (2020) 467–483.

[65] W.-J. Xu, X.-Y. Dong, Simulation and verification of landslide tsunamis using a 3d sph-dem coupling method, Computers and Geotechnics 129 (2021) 103803.

[66] B. E. Snelling, G. S. Collins, M. D. Piggott, S. J. Neethling, Improvements to a smooth particle hydrodynamics simulator for investigating submarine landslide generated waves, International Journal for Numerical Methods in Fluids 92 (7) (2020) 744–764.

[67] T. Kärnä, S. C. Kramer, L. Mitchell, D. A. Ham, M. D. Piggott, A. M. Baptista, Thetis coastal ocean model: discontinuous Galerkin discretization for the three-dimensional hydrostatic equations, Geoscientific Model Development 11 (2018) 4359–4382. doi:10.5194/gmd-11-4359-2018.

[68] W. Pan, S. C. Kramer, M. D. Piggott, Multi-layer non-hydrostatic free surface modelling using the discontinuous galerkin method, Ocean Modelling 134 (2019) 68–83.

[69] M. C. Clare, J. R. Percival, A. Angeloudis, C. J. Cotter, M. D. Piggott, Hydromorphodynamics 2d modelling using a discontinuous galerkin discretisation, Computers & Geosciences 146 (2020) 104658.

[70] S. Bunya, E. J. Kubatko, J. J. Westerink, C. Dawson, A wetting and drying treatment for the runge–kutta discontinuous galerkin solution to the shallow water equations, Computer Methods in Applied Mechanics and Engineering 198 (17-20) (2009) 1548–1562.

[71] S. Vater, N. Beisiegel, J. Behrens, A limiter-based well-balanced discontinuous galerkin method for shallow-water flows with wetting and drying: Triangular grids, International Journal for Numerical Methods in Fluids 91 (8) (2019) 395–418.

[72] E. F. Toro, Riemann solvers and numerical methods for fluid dynamics: a practical introduction, Springer Science & Business Media, 2013.

[73] R. M. Iverson, R. P. Denlinger, Flow of variably fluidized granular masses across three-dimensional terrain: 1. coulomb mixture theory, Journal of Geophysical Research: Solid Earth 106 (B1) (2001) 537–552.

[74] N. A. Phillips, A coordinate system having some special advantages for numerical forecasting, Journal of Meteorology 14 (2) (1957) 184–185.

[75] P. Lin, C. Li, A σ-coordinate three-dimensional numerical model for surface wave propagation, International Journal for Numerical Methods in Fluids 38 (11) (2002) 1045–1068.

[76] R. Comblen, J. Lambrechts, J.-F. Remacle, V. Legat, Practical evaluation of five partly discontinuous finite element pairs for the non-conservative shallow water equations, International Journal for Numerical Methods in Fluids 63 (6) (2010) 701–724.

[77] A. Harten, P. D. Lax, B. v. Leer, On upstream differencing and godunov-type schemes for hyperbolic conservation laws, SIAM review 25 (1) (1983) 35–61.

[78] S. Néelz, et al., Desktop review of 2D hydraulic modelling packages, Bristol: Environment Agency, 2009.

[79] S. Yavari-Ramshe, B. Ataie-Ashtiani, B. F. Sanders, A robust finite volume model to simulate granular flows, Computers & Geotechnics 66 (MAY) (2015) 96–112.

[80] P. Batten, N. Clarke, C. Lambert, D. M. Causon, On the choice of wavespeeds for the hllc riemann solver, SIAM Journal on Scientific Computing 18 (6) (1997) 1553–1570.

[81] A. Harten, P. D. Lax, A random choice finite difference scheme for hyperbolic conservation laws, SIAM Journal on Numerical Analysis 18 (2) (1981) 289–315.

[82] E. F. Toro, M. Spruce, W. Speares, Restoration of the contact surface in the hll-riemann solver, Shock waves 4 (1) (1994) 25–34.

[83] S. Gottlieb, C.-W. Shu, Total variation diminishing runge-kutta schemes, Mathematics of computation of the American Mathematical Society 67 (221) (1998) 73–85.

[84] T. Kärnä, V. Legat, E. Deleersnijder, A baroclinic discontinuous Galerkin finite element model for coastal flows, Ocean Modelling 61 (2013) 1–20.

[85] H. Cui, J. Pietrzak, G. Stelling, A finite volume analogue of the p1nc-p1 finite element: With accurate flooding and drying, Ocean Modelling 35 (1-2) (2010) 16–30.

[86] M. Zijlema, G. Stelling, P. Smit, Swash: An operational public domain code for simulating wave fields and rapidly varied flows in coastal waters, Coastal Engineering 58 (10) (2011) 992–1012.

[87] G. Ma, F. Shi, J. T. Kirby, Shock-capturing non-hydrostatic model for fully dispersive surface wave processes, Ocean Modelling 43 (2012) 22–35.

[88] T. Kärnä, B. De Brye, O. Gourgue, J. Lambrechts, R. Comblen, V. Legat, E. Deleersnijder, A fully implicit wetting–drying method for dg-fem shallow water models, with an application to the scheldt estuary, Computer Methods in Applied Mechanics and Engineering 200 (5-8) (2011) 509–524.

[89] A. Mangeney, P. Heinrich, R. Roche, Analytical solution for testing debris avalanche numerical models, Pure and Applied Geophysics 157 (6-8) (2000) 1081–1096.

[90] K. Hutter, T. Koch, C. Pluüss, S. B. Savage, The dynamics of avalanches of granular materials from initiation to runout. part ii. experiments, Acta Mechanica 109 (1) (1995) 127–165.

[91] O. Hunger, N. Morgenstern, Experiments on the flow behaviour of granular materials at high velocity in an open channel, Geotechnique 34 (3) (1984) 405–413.

[92] O. Hungr, Simplified models of spreading flow of dry granular material, Canadian Geotechnical Journal 45 (8) (2008) 1156–1168.

[93] V. Heller, W. H. Hager, Impulse product parameter in landslide generated impulse waves, Journal of waterway, port, coastal, and ocean engineering 136 (3) (2010) 145–155.

[94] V. Heller, Landslide generated impulse waves: Prediction of near field characteristics, Ph.D. thesis, ETH Zurich (2007).

[95] F. Mohammed, Physical modeling of tsunamis generated by three-dimensional deformable granular landslides, Ph.D. thesis, Georgia Institute of Technology (2010).